Nanoscale

Layer-by-Layer Assembly in Nanochannels: Assembly Mechanism and Applications

Journal:	*Nanoscale*
Manuscript ID	NR-REV-02-2021-001113.R1
Article Type:	Review Article
Date Submitted by the Author:	09-Apr-2021
Complete List of Authors:	Zhang, Shouwei; China University of Geosciences, Xia, Fan; China University of Geosciences, Materials Science and Chemistry Demoustier-Champagne, Sophie; Universite catholique de Louvain Ecole Polytechnique de Louvain, Jonas, Alain; Universite Catholique de Louvain, Institute of Condensed Matter and Nanosciences

Layer-by-Layer Assembly in Nanochannels: Assembly Mechanism and Applications

Shouwei Zhang[a], Fan Xia[a], Sophie Demoustier-Champagne[b], Alain M. Jonas*[b]*

[a]Faculty of Materials Science and Chemistry, China University of Geosciences, 430074 Wuhan, China

[b]Institute of Condensed Matter and Nanosciences - Bio and Soft Matter (IMCN/BSMA), Université Catholique de Louvain, Croix du Sud 1/L7.04.02, B1348 Louvain-la-Neuve, Belgium

Email: sophie.Demoustier@uclouvain.be; alain.jonas@uclouvain.be.

Key words: Layer-by-layer, Nanochannels, Assembly mechanism, Liberated nanotubes, Nanotube arrays, Membrane-based fluidics.

Abstract: Layer-by-layer (LbL) assembly is a versatile technology to construct multifunctional nanomaterials using various supporting substrates, enabled by the large selection freedom of building materials and diversity of possible driving forces. The fine regulation over the film thickness and structure provides an elegant way to tune the physical/chemical properties by mild assembly conditions (e.g. pH, ion strength). In this review, we focus on LbL in nanochannels, which exhibit a different growth mechanism compared to "open", convex substrates. The assembly mechanism in nanochannels is discussed in detail, followed by the summary of applications of LbL assemblies liberated from nanochannel templates which can be used as nanoreactors, drug carriers and transporting channels across cell membranes. For fluidic applications, robust membrane substrates are required to keep in place nanotube arrays for membrane-based separation, purification, biosensing and energy harvesting, which are also discussed. The good compatibility of LbL with crossover technologies from other fields allows researchers to further extend this technology to a broader range of research fields, which is expected to result in an increased number of applications of LbL technology in the future.

1. Introduction

The deposition of a functional nanocoating is a facile and efficient way to adjust the interaction of materials with their environment in a controlled way, leading to smart multifunctional hybrid materials in which the interface and bulk of the material are engineered independently[1]. For example, the bulk material can be used as a mechanically-robust support, while the surface coating provides specific properties for a useful task. Scientists and engineers have developed different methods to implement functional coatings, including Langmuir-Blodgett (LB)[2], sputtering[3], electroplating[4], self-assembly of monolayers[5], adsorption or growth of polymer brushes[6-12], and layer-by-layer assembly. These are variously selected depending on the coating materials and purpose of the coating: trivial examples are zinc which is electroplated on iron materials to prevent corrosion, and biomacromolecules which are layer-by-layer assembled on implants to improve biocompatibility.

Among these methods, layer-by-layer assembly appears to be an especially simple and versatile strategy to prepare nanocoatings; it was first proposed in 1966 by Iler[13] who constructed multilayer assemblies via alternating adsorption of anionic and cationic colloidal particles. Since Decher and co-workers[14, 15] rejuvenated and adapted this concept to the formation of ultrathin multilayer films using bipolar amphiphiles and polyelectrolytes in 1991, LbL technology has been extensively studied. Nowadays, it is a well-established and versatile method for the construction of nanocoatings whose thickness, composition, structure and properties can be tailored by tuning assembly conditions[16]. The key competitive features of LbL are its mild aqueous assembly conditions, the absence of sophisticated and expensive equipment, the large freedom in selecting building materials, and the diverse driving forces for material assembly.

Different strategies were exploited to achieve layer-by-layer assembly, including dipping, filtration, spinning, spraying, electromagnetically-controlled assembly, and fluidic assembly[1]. The dipping assembly is especially suitable for the coating of the inner porosity of porous substrates used for the fabrication of smart membranes and of functional nanoobjects, since the aqueous solution can get access to deeply-buried surfaces within the porous structure; this cannot be easily achieved by other technologies. LbL-modified nanoporous membranes can be used as functional fluidic devices for performing specific tasks. Furthermore, since coating the

pores of such membranes replicates their shape, the resulting templated assemblies can be liberated by dissolution of the membranes to create tubular-shaped nanostructures displaying a high loading capacity and a long circulation persistence in vivo[17].

In this review, we only focus on dipping- and filtration-based layer-by-layer assembly, which are compatible with nanoporous membranes. Compared to planar surfaces ("open system"), the nanochannels of a membrane nanoconfine the assembly mechanism, which therefore differs from the one observed on flat surfaces[18]. The fabrication of nanochannel membranes and the basics of dipping-based layer-by-layer assembly are first introduced with a focus on the diversity of building components, driving forces, and parameters that tune the physical and chemical properties of nanofilms; this is followed by a discussion of the mechanism of LbL assembly in nanochannels. Finally, recent progresses in LbL-in-membrane applications are summarized to show its practical interest in different fields, such as biosensing, drug-targeted delivery, energy conversion, seawater desalting and molecule/ion separation.

2. Nanochannel membranes

Progresses in nanofabrication and nanotechnology have enable the fabrication of stable solid-state nanochannels (Figure 1A-C) in membranes[19] which can be employed in membrane science or as templates to fabricate functional nanotubes/nanorods.

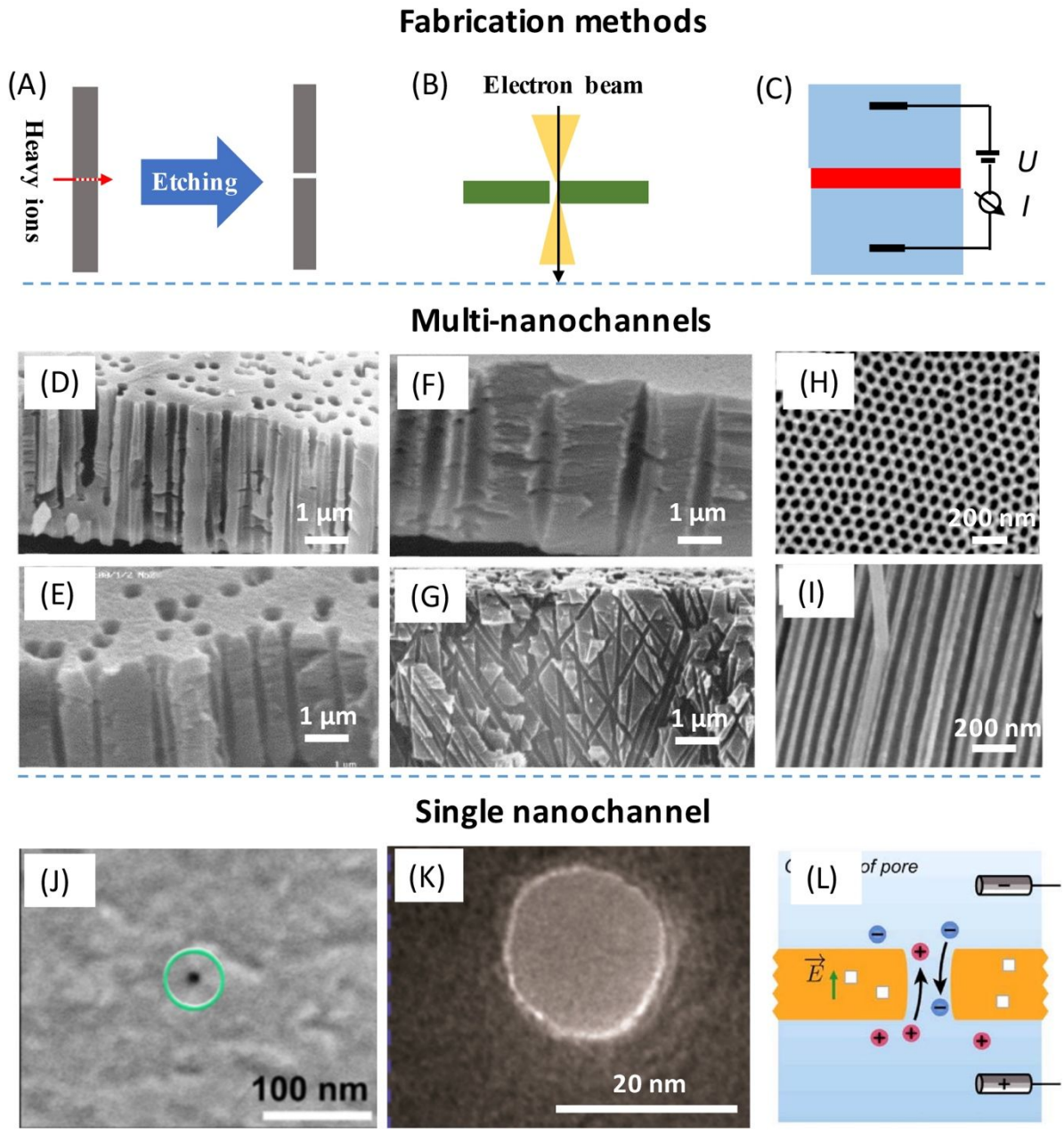

Figure 1. Fabrication methods and resulting nanochannel structures. (A) Ion-track etching, (B) electron beam lithography, and (C) electrochemical etching approaches were employed to create (D-I) multi and (J-L) single nanochannel(s) through entire polymer and inorganic membranes. Ion-track etched polymer membranes possessing multi-channels with (D) cylindric, (E) "bow-tie", (F) cigar-like, and (G) intersected nanochannel structures[20]. Adapted with permission from ref. 20. Copyright 2001 Elsevier. (H) Top and side (I) view of AAO nanochannel membranes[21]. Adapted with permission from ref. 21. Copyright 2010 Elsevier. (J) Polymer single nanochannel achieved using single ion track technology[22] (Reprinted with

permission from ref. 22. Copyright 2016 American Chemical Society) and (K) silicon nitride single nanochannel fabricated using TEM electron beam lithography[23] (Adapted with permission from ref. 23. Copyright 2018 American Chemical Society). (L) Illustration of nanochannel formation using controlled dielectric breakdown[24] (Reprinted with permission from ref. 24. Copyright 2014 Public Library of Science).

Porous organic and inorganic membranes, such as polymer membranes and anodic aluminum oxide (AAO) plates, are commercially available. Track-etched polymer membranes with randomly positioned nanochannels are fabricated in two steps, starting from the bombardment with heavy energetic ions of raw polymer foils having a thickness ranging from a few microns to a few tens of microns, followed by subsequent removal of the degraded polymers in latent tracks by wet-chemical etching, producing the channels inside the polymer matrix[25]. Polycarbonate (PC), polyethylene terephthalate (PET), and polyimide (PI) materials are commonly employed as polymer matrix. Based on this ion-track technology, pore size, shape and density can be varied in a controllable manner by the proper selection of the conditions under which irradiation and post-treatment procedures are carried out (Figure 1D-G). Pore size can be tuned from 10 nanometers to a few micrometers, offering a promising platform for functional membranes and for fabricating nano-objects with extremely high aspect ratios. The desired pore density can be obtained by controlling process parameters; however, the highest density is limited by pore size, owing to their random distribution in polymer membranes. The larger the pore size, the lower the highest pore density that can be reached due to the increasing possibility of interconnection among vertically aligned channels. Typically, for a pore size of 200 nm, a pore density up to 10^8 cm^{-2} can be reached while, for a 1 μm pore size, the highest possible pore density is limited to 10^6 cm^{-2}. Moreover, intersected nanochannel PC templates can be obtained by a sequential two-step exposure to energetic heavy ions, at different incidence angles with respect to the normal to the polymer membrane surface[26-30]. In contrast, porous AAO plates, fabricated by anodizing high purity Al foils under appropriate voltage, have vertically aligned and well-packed cylindrical nanochannels with diameters ranging from 5 to 400 nm (Figure 1H-I). The pore diameters and interpore distances of AAO template can be adjusted by changing anodic oxidization parameters[21].

In an extreme case, a single nanochannel has been achieved, using single ion track in polymer foils. Other technologies such as electron beam lithography[31, 32] and dielectric breakdown[24, 32] are also developed to make a channel in polymer or inorganic thin films (e.g., poly(dimethylsiloxane), silicon nitride, silicon dioxide, and silicon) (Figure 1J-L). Such single nanochannels are perfect candidates to mimic biological ion nanochannels for analytical applications[33], enabling the mechanism of ion transport to be well-studied, since the influence of neighboring nanochannels existing in multi-channel membranes can be eliminated, contributing to an improved selectivity and sensitivity in analytical applications. Single ion track polymer foils were widely employed to fabricate single nanochannels for various applications[34, 35] because their shape and size can be tuned in a controlled way by selection of appropriate etching conditions[36-39].

3. Layer-by-Layer assembly

Layer-by-layer assembly is a simple and flexible technique that is compatible with other methods[40], such as spin coating, spraying, centrifugation, electrodeposition, and vacuum/pressure assisted filtration, depending on the different processing requirements associated with substrates. In this review, we focus on porous membranes having vertically aligned micro/nano channels. For this kind of supporting substrates, dipping and vacuum/pressure assisted filtration are suitable for the formation of nanofilms in channels; tunable parameters, related issues in the process, and mechanism of LbL assembly are discussed in following sections.

3.1 Basics of LbL assembly

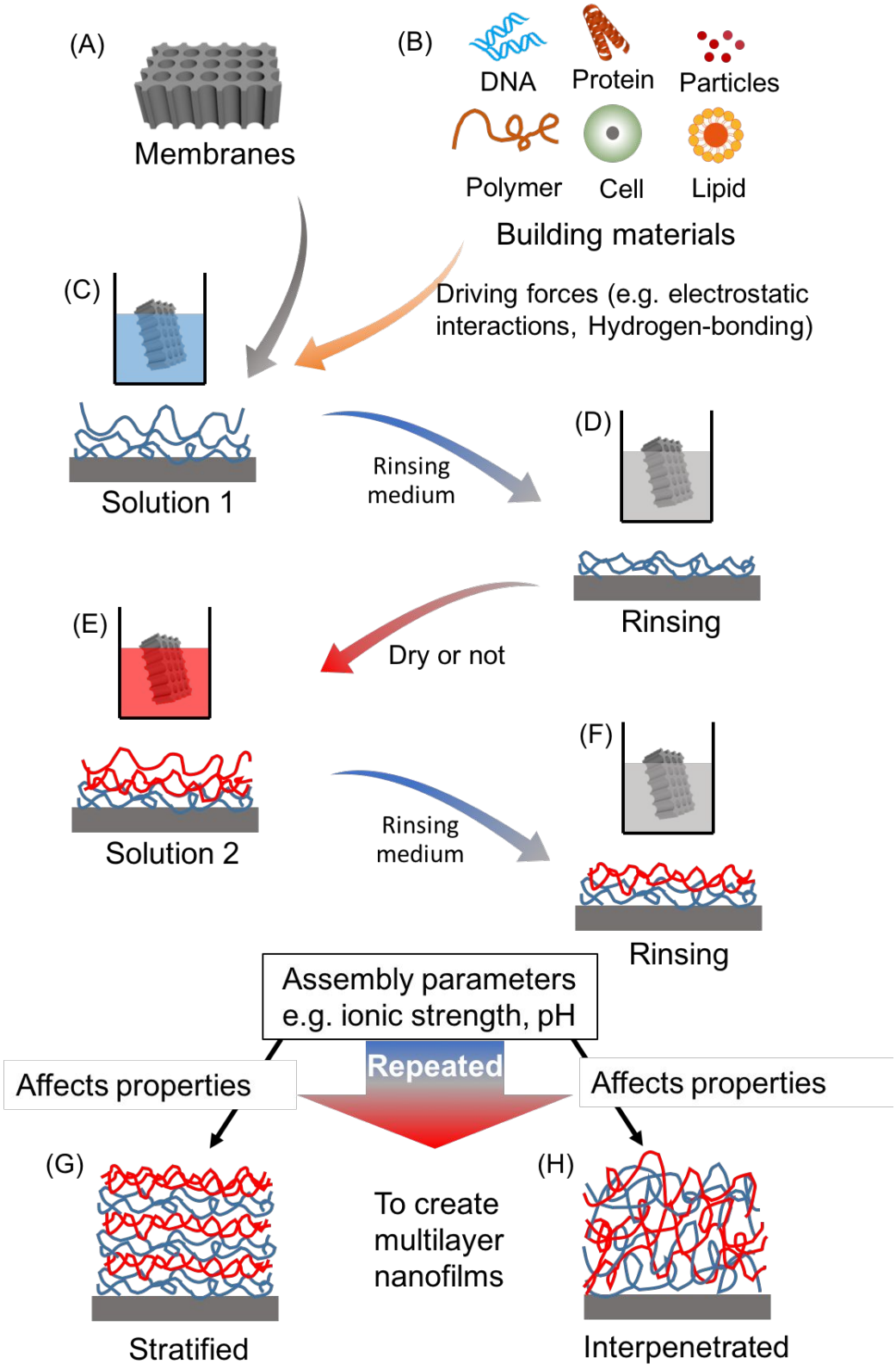

Figure 2. Schematic representation of layer-by-layer adsorption processes (dipping) in the channels of a membrane (A), for diverse building materials (B). The porous membrane is immersed in solution 1 (C) followed by a rinsing step to remove loosely attached

polyelectrolyte chains (D). Then the modified nanochannel is transferred to solution 2 (E), followed by another rinsing step (F).

Thanks to the mild assembly condition (aqueous solution), a diversity of useful materials including nanofibers[41-43] and synthetic[44-46] and natural ones[47-50] (for instance, cell, bioactive enzymes) can be incorporated into LbL nanofilms as both scaffold and functional components, distinguishing LbL assembly for fabricating smart multifunctional nanocoating (Figure 2). Polyelectrolytes are the most commonly and widely used materials to construct functional nanofilms based on electrostatic interactions, possibly combined with hydrogen-bonding when the polymers carry hydrogen donor and acceptor moieties. Here, we take polyelectrolytes as example to describe the layer-by-layer assembly process on negatively-charged nanochannels; this buildup process involves the alternating deposition of two oppositely charged polymers with intermediate rinsing steps to remove unbound and loosely attached polymer chains. The first adsorption of the polycation results in surface charge reversal, as a result of charge overcompensation, facilitating the following deposition of polyanion chains to finalize one cycle. This whole cycle is repeated until the desired number of bilayers is reached.

A unique feature of the LbL assembly is its ability to control film growth at the nanoscale with respect to the thickness, internal and surface composition and structure, and therefore related properties, by simply manipulating the assembly parameters and buildup protocols[16, 51-53]. pH, ionic strength, temperature, and the nature of solvent are commonly tunable parameters. pH is especially effective for weak polyelectrolytes and proteins which have an isoelectric point. The charge polarity and charge density along polymer chains are indeed regulated by pH. For strong polyelectrolytes, a high ionic strength can effectively screen the repulsion between neighboring charged groups, leading to more coiled conformations of polymer chains and consequently thicker polyelectrolyte layers compared to the more stretched polymer chains in solutions of low ionic strength (Figure 2G). The coiled polymer chains facilitate the interpenetration between adjacent layers, favoring the formation of homogeneous structures (Figure 2H), while more stretched chains lead to more stratified film structures (Figure 2G). Elevated temperatures cause the swelling of previously adsorbed films and allow for increased trapping of polymers from the bulk solution into the already-formed film, resulting in much

thicker films than when deposited at room temperature[54]. The solvent quality from which polyelectrolytes are adsorbed also affects film growth and properties (e.g., swelling, stability) [55]. Unfavorable segment-solvent interactions in a poor solvent result in the formation of progressively thicker films and enhanced stability against high ionic strength. Apart from these solution parameters, the rinsing medium and whether the film is dried or not after each rinsing step are also influential factors in most cases[56]. Besides typical electrostatic interactions and hydrogen bonds, various other types of interactions were also exploited for LbL assembly, including hydrophobic interactions[57], charge transfer[58], host-guest interactions[59], covalent bonds[60], and bio-specific recognition[61-65], depending on the nature of building materials, thus demonstrating the compatibility of the method with a wide range of materials. Moreover, the assembly medium can be extended to organic solvents by using specific interaction mechanisms having a high affinity in these solvents, such as the interaction between amine moieties and metal nanoparticles in organic media. Amine-functionalized materials[66-68], including polyamide, dendrimers, or small molecules have been employed to construct stable nanoparticle films by self-assembly with ligand-stabilized metal nanoparticles, using ligand exchange[69]. Compared to conventional LbL, the ligand-mediated LbL assembly involves ligand replacement by amine-functionalized molecules (Figure 3), due to the higher affinity of amine groups toward metal nanoparticles than the ligand stabilizers. The distance between adjacent metal nanoparticles can be tuned by the size of amine-bearing molecules, yielding nanoparticle films with tunable properties. For instance when a small molecule, tris(2-aminoethyl) amine (TREN) was applied in ligand-mediated LbL assembly of tetraoctylammonium bromide (TOABr)-stabilized Au NPs, the formation of only one TREN molecule layer between the adjacent Au NP layers significantly reduced the contact resistance between neighboring NPs (Figure 3) and, consequently, imparted electrical properties similar to those of bulk Au films.

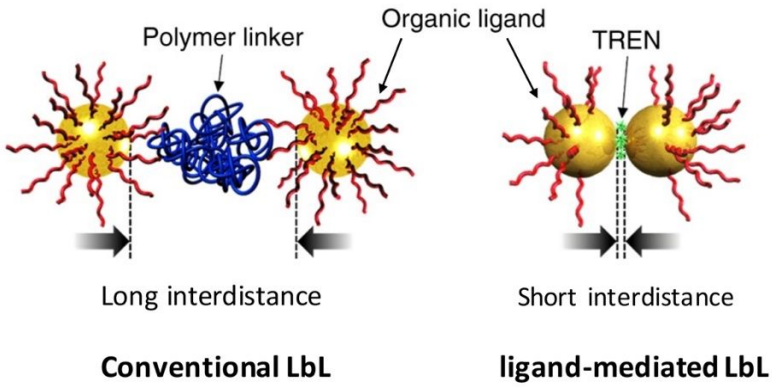

Figure 3. Schematic illustration for different nanoparticle-based LbL structures made by traditional LbL assembly (based on electrostatic interactions, hydrogen bonding, or covalent bonding) and ligand-mediated LbL assembly.[67] TREN: tris(2-aminoethyl) amine. Adapted with permission from ref. 67. Copyright 2017 Springer Nature.

3.2 Assembly mechanism in nanochannels

The effect of nanoconfinement on the conformations of polymer chains has been reported[70-73]. The LbL growth mechanism in confined geometries is significantly different from that in "open space"[74, 75] and has been studied by using a well-known polyelectrolyte system, the poly(allylamine hydrochloride) PAH/PSS pair[18]. This study revealed the existence of two different regimes related to the growth kinetic with a transition point occurring at around 70% of pore filling. In the first regime, a growth mechanism similar to the one on planar substrates, including the effect of ionic strength and pH, was observed. As pore size decreases with the build-up of LbL multilayers, the LbL growth enters into the second regime, which is kinetically much slower, due to the formation of an entangled polyelectrolyte network inside the pores. The resulting limitation in the diffusion of polyelectrolytes into the pores leads to a slowed growth in terms of thickness increment per cycle of deposition. The pore size is a significant factor in the LbL buildup. As shown in Figure 4A, in very small pores (about 100 nm), it takes only a few LbL cycles to fill the pores and enter into the slower growth regime (regime 2), while reaching this transition requires more LbL deposition cycles in larger pores.

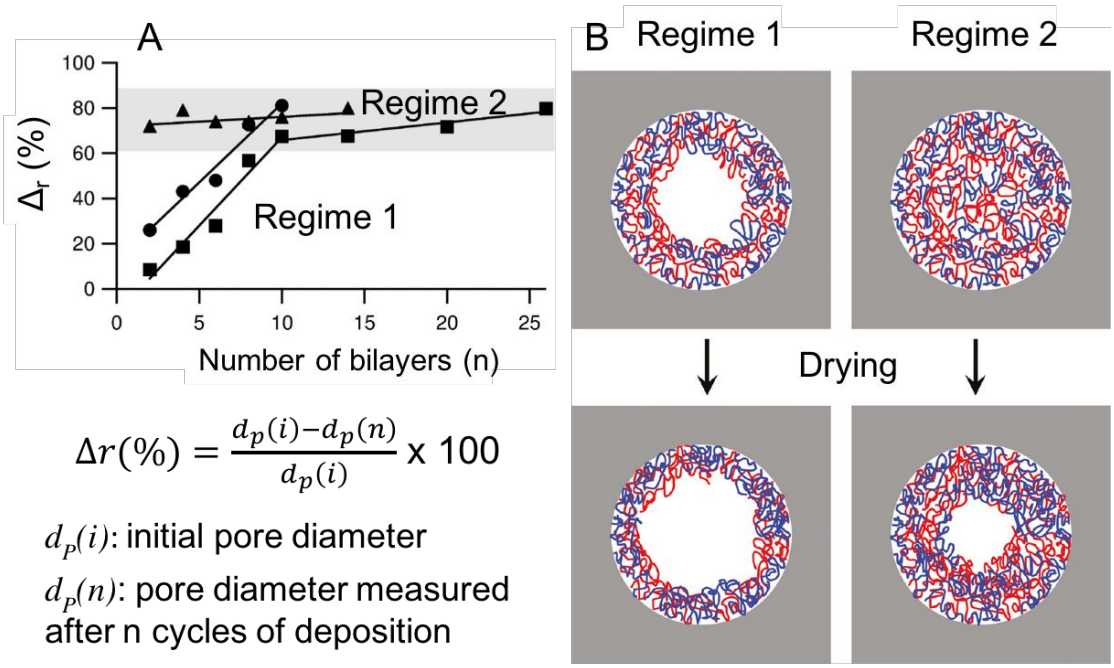

Figure 4. LbL growth evolution (Δr) of PAH/PSS multilayers as a function of the number of bilayers (n) in pores of 100 nm (triangles), 200 nm (circles), and 500 nm (squares) diameter (A), and proposed growth mechanism consisting of two different two regimes (B).[18] Adapted with permission from ref. 18. Copyright 2010 American Chemical Society.

Cho and coworkers[76] investigated the effect of pore size on the formation of tubular structures within AAO templates. A particular attention was paid to the comparison of thickness increment per bilayer between pores of different sizes and flat substrates for LbL assembly carried out under identical conditions. According to the mechanism proposed above (Figure 4), in all studied cases, the LbL growth was in regime I, since the value of Δr (defined in Figure 4) for 30 bilayers was around 30% for all AAO templates, far below the transition point. In small pores (30-345 nm), the thickness of tube walls was found to be thinner than that of planar film built on silicon substrates under similar conditions (Figure 5), regardless the size of polyelectrolytes as well as assembly conditions[74, 76-79]. The authors attributed this difference of thickness to hindered polyelectrolyte chain diffusion into the pores, called an entropic entry barrier; when the pore diameter increases and approaches 430 nm, a wall thickness similar to the LbL film on a flat substrate was obtained (Figure 5B, C) [76]. However, the smaller the polyelectrolyte coils (of size tuned by adding electrolyte salt and adjusting pH), the higher the

ratio of nanotube wall thickness to that of a flat film, for a given small pore size. The value of this ratio increased from 0.33 up to 0.7 in 70 nm nanopores when the pH of the PAH solution was adjusted from 4-5 to 9.3-9.5. The same phenomenon was observed for all pores presenting a diameter below 100 nm, when the ionic strength was increased. This increase of polyelectrolyte solution pH and ionic strength reduces the size of pH and salt-sensitive polyelectrolyte coils, respectively, by reducing the charge density and screening the repulsive interactions between charged units along the chains.

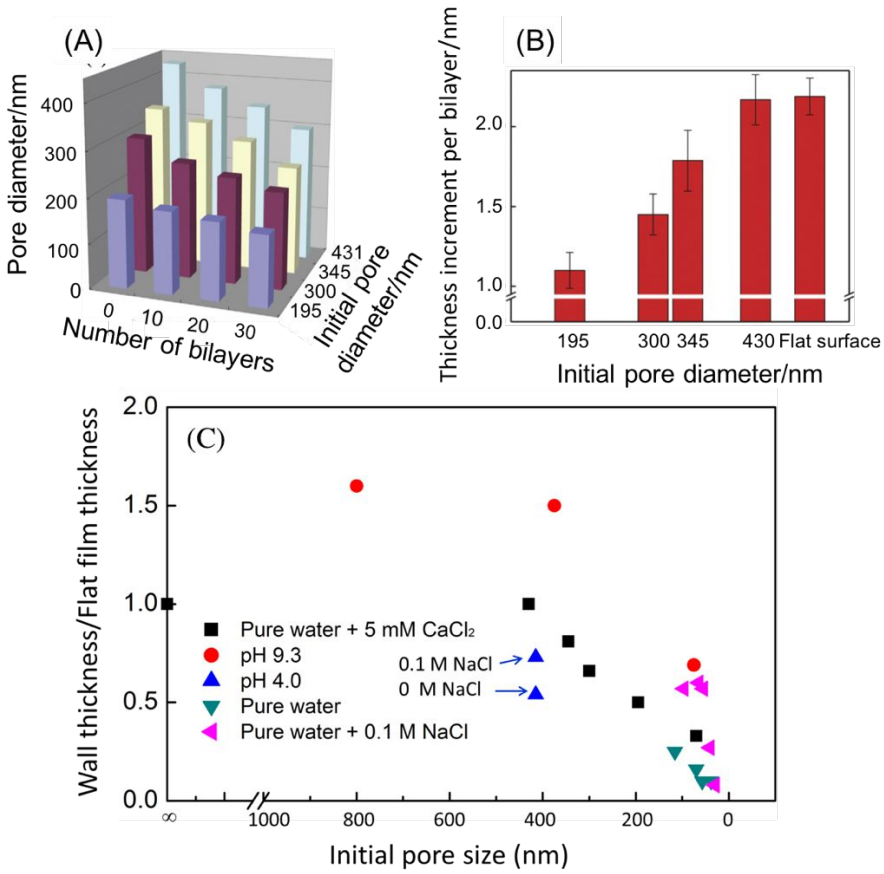

Figure 5. (A) Evolution of the size of the open lumen of pores of AAO templates of various initial pore diameters, as a function of the number of deposited PAH/PSS bilayers (obtained from SEM images), (B) average thickness of one (PAH/PSS) bilayer assembled in various AAO templates with different initial pore diameters[76], (C) same as B after division by the thickness of the thickness of the polyelectrolyte bilayer grown over flat substrates under identical assembly conditions. The various LbL assembly conditions used to study the influence of pH and ionic strength on the growth behavior in nanochannels are summarized in (C). ■[76, 78], ●[77, 80] and ▲[79] represent the PAH/PSS system, while ▼[74] and ◀[74] indicate that 4th generation

polyanion and polycation dendrimers were used for LbL assembly. Images (A, B) were adapted with permission from ref. 76. Copyright 2014 Elsevier.

LbL assembly in nanochannels exhibits thus a strong dependence on pH, ionic strength of polyelectrolyte solutions and nature of polyelectrolyte pairs, as observed for planar surfaces. The properties of polymer materials influence multilayer buildup significantly. For the PAH/PSS pair, the ratio with respect to the increment per bilayer in regime 1 evolves from 0.54 to 1.5, in *ca.* 400 nm nanopores, in response to the increase of pH and ionic strength. The same trend appears under one specific assembly condition when the initial pore size increases gradually within an appropriate range. However, a LbL growth comparable to what occurs on a flat surface is expected when the pore size increases up to a lower limit (point at which the confinement of pores can be ignored). This means that depending on the assembly conditions, there is a critical pore size from which the LbL growth behavior is identical to that on the 'open' planar surface (Figure 5C, wall thickness/flat film thickness ratio =1). For instance, this critical pore size is *ca.* 200 nm and 400 nm for LbL growth from solutions at pH 9.0 and pure water with 5 mM $CaCl_2$, respectively. The presence of this interesting behavior results from a compromise between various effects, either facilitating or hindering the polyelectrolyte adsorption in nanopores, such as incomplete drainage [80], curvature of pores [81], confinement effect [18, 76, 77], and depletion effect [79].

Apart from the conventional dipping route, pressure or vacuum can be used to assist the adsorption of polyelectrolytes. When using this process for the construction of nanotubes, cationic and anionic polyelectrolyte solutions are alternatively filtered through the nanoporous membranes [81]. The filtration-based LbL process has been extensively investigated by Jonas and coworkers [82] who deposited a pair of strong polyelectrolytes within a series of track-etched nanoporous PC membranes, with pore size ranging from 50 to 850 nm, under various assembly conditions. The results show that when filtration-LbL assembly is performed, the pores are rapidly filled by a dense gel for a very limited number of deposition cycles, depending on the initial pore size. The increment of thickness per cycle of deposition is much larger than on flat surfaces (increasing by a factor of one hundred, in some cases), resulting from the entanglement

of the polyelectrolyte chains which are in a concentrated regime when passing in the confined channels.

Regardless of the methodology used for polyelectrolyte adsorption (filtration or immersion), one important issue during LbL deposition within nanopores is that LbL assembly also occurs on the top and bottom faces of the membrane, leading to the formation of a crust over the template surfaces. This crust may cover the pores, causing restriction in LbL growth within the nanochannels when increasing the number of bilayers. This surface film must therefore be removed after each or several bilayer depositions when membranes with narrow pores are used as templates. This decrusting treatment is also required at the end of the buildup process in order to separate the nanotubes/wires. Various methods have been used to eliminate those LbL films, including plasma etching [83], polishing with alumina powder [84] and scratching with a cotton swab [18, 85]. However, in some cases there is no need to eliminate the surface functional layer, because they may also have an important contribution to the functions of modified membranes, depending on the aim that researchers want to achieve.

As discussed above, LbL assembly in nanochannel involves polymer chain diffusion and assembly under confinement. In particular, the polymer chains experience considerable restriction to diffusion in regime 2 (Figure 4B). To further establish the role of confinement on LbL film growth, it is instructive to briefly discuss LbL assembly on nanopatterned surfaces for which only lateral confinement happens; thus a different behavior is expected, potentially bridging LbL over flat surfaces and in nanopores. There are typically two ways to laterally confine polyelectrolytes during adsorption, depending on the nature of nanopatterned surfaces. One is achieved by using flat surfaces with different functional regions that have distinct affinities to polyelectrolytes, resulting in nanoconfined deposition of polyelectrolytes on specific nanoscale-spots (Figure 6A). Another way is by employing a lift-off strategy combined with a nanolithography method such as electron beam or nanoimprint lithography. In this case, the LbL-assembled multilayer first adsorbs on both the resist and open regions of the substrate which have a nanoscale dimension (Figure 6F); in a subsequent step, the layer adsorbed on the resist is eliminated in a lift-off process. The extent of confinement is related to the size of the exposed area in the resist relative to the one of the polyelectrolyte chains; therefore, it is not surprising that no specific confinement effect is observed in microscale gaps[75, 86]. Nevertheless,

it has been reported that confinement may become effective in micro-imprinted substrates in the presence in solution of polyelectrolyte aggregates resulting from a high ionic strength[86].

Interestingly, flat LbL films can also be patterned by solvent-assisted capillary molding[87] or embossing with a hard mold[88, 89], to create a surface pattern. However, these processes belong to the category of post-treatment of LbL films for specific applications rather than LbL assembly under confinement, and are thus not reviewed here.

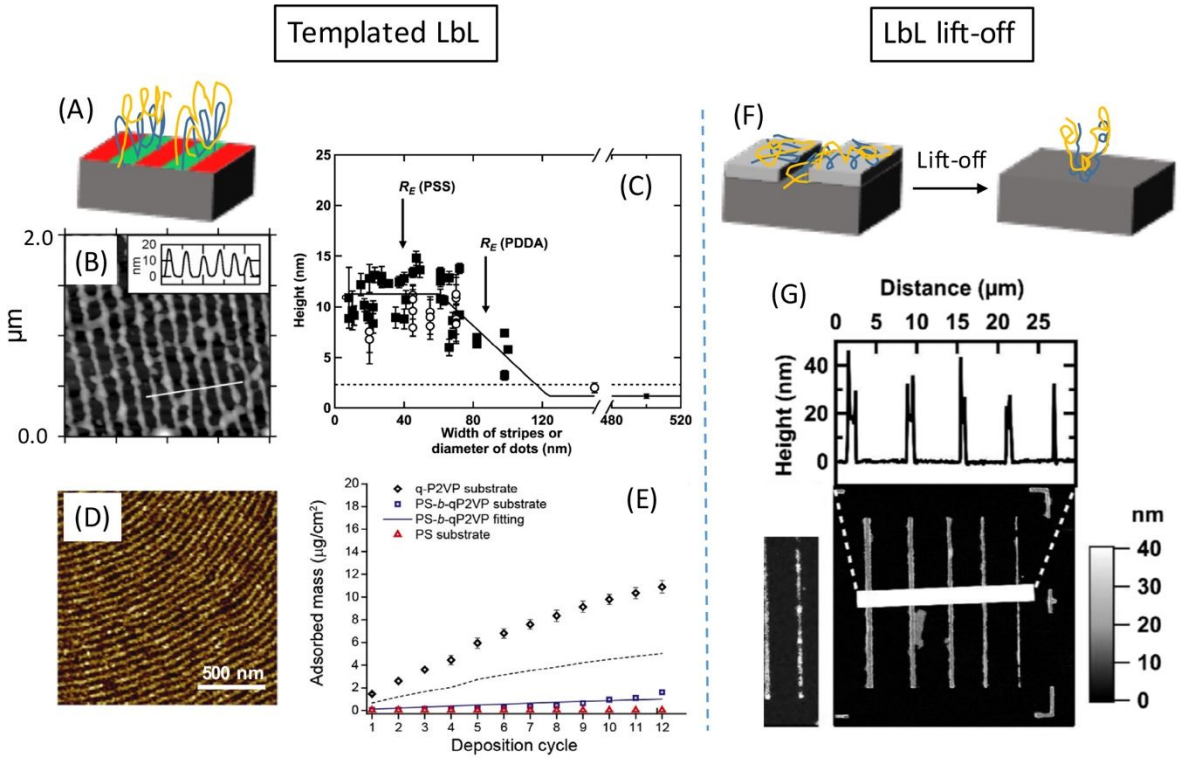

Figure 6. LbL assembled on nanopatterned surfaces via templated LbL and LbL lift-off approaches. (A) Illustration of LbL multilayers on chemically nanopatterned substrate. (B) AFM images of $(PDDA/PSS)_5$ films on binary nanopatterned surface prepared from a hydrophobic alkane-silane in a background of hydrophilic oligo(ethylene glycol) (OEG)-silane. PDDA: Poly(diallyldimethylammonium chloride), PSS: Poly(styrene sodium sulfonate). (C) Thickness of $(PDDA/PSS)_5$ LbL multilayers, grown at pH 3 on hydrophobic alkanesilane stripes (squares) or dots (circles) in an OEG-silane hydrophilic background[75]. The dashed line is the thickness of the laterally-infinite multilayer. Arrows indicate the average end-to-end distance of the PSS and PDDA chains in solution. Reprinted with permission from ref. 75. Copyright 2006 Wiley-VCH Verlag GmbH & Co. KGaA, Weinheim. (D) AFM image of

$(PDDA/PSS)_{10}$ multilayers assembled in salt-free solution on a quaternized polystyrene-block-poly(2-vinylpyridine) (PS-*b*-qP2VP) block copolymer thin film. (E) Calculated mass of polyelectrolyte adsorbed on homopolymer substrate and PS-*b*-qP2VP template from QCM-D measurements[90]. Dashed line corresponds to the expected amount of adsorbed mass based on the adsorption on qP2VP homopolymer (black data points) multiplied by the calculated surface fraction of qP2VP domains (0.46). Adapted with permission from ref. 90. Copyright 2017 Elsevier. (F) Illustration of LbL multilayers prepared by lift-off strategy. (G) AFM image of lifted-off $(PVBTAC/PSS)_5$ LbL film; a height profile was drawn along the thick white line to show the thickness[91]. PVBTAC: Poly(vinylbenzyltrimethylammonium chloride). Reprinted with permission from ref. 91. Copyright 2012 Wiley-VCH Verlag GmbH & Co. KGaA, Weinheim.

Research work concerning polyelectrolyte LbL assembly on flat nanopatterned substrates is scarce[75, 90-95]. The first example was reported by Jonas et al.[75] who studied the effect of nanoconfinement on LbL multilayer growth using binary nanopatterned surfaces prepared by electron beam lithography and gas-phase silanation. Nanopatterned stripes or dots were functionalized with a hydrophobic alkanesilane monolayer, and hydrophilic oligo(ethylene glycol)-silane was employed to cover residual background substrate, facilitating the nanoconfined deposition of PDDA/PSS polyelectrolytes on the hydrophobic regions while neighboring oligo(ethylene glycol)-silane brushes repelled PDDA/PSS (Figure 6B). The thickness of $(PDDA/PSS)_5$ multilayer assembled on nanopatterned surface was four to five times larger than on laterally-infinite substrate when the width of nanostripes or diameter of dots was smaller or comparable to the size of polyelectrolytes in solution (Figure 6C), revealing that the lateral nanoconfinement effect had a significant influence in terms of polyelectrolyte chain conformation. The higher thickness of multilayers on nanoconfined surface results from the more coiled conformation of polyelectrolyte chains when adsorbing over regions of size smaller than the unperturbed size of the coils in solution.

LbL assembly over block copolymer nanopatterned templates was also investigated, giving rise to a different behavior.[90] Poly(2-vinylpyridine) (P2VP) domains were crosslinked by 1,4-diiodobutane (DIB) not only to improve the stability of polystyrene-block-poly(2-

vinylpyridine) (PS-*b*-qP2VP) block copolymer film against swelling but also to quaternize the P2VP and thereby form positive charged qP2VP regions for LbL assembly. As shown in Figure 6D, in salt-free solution, the $(PDDA/PSS)_{10}$ multilayers were confined to the qP2VP domains (*ca.* 40 nm in width), consistent with the fast film growth observed on homogeneous qP2VP substrate and undetectable growth seen on homogeneous PS substrate (Figure 6E). An increased of the ionic strength of the solution reduces the adsorption selectivity on PS-*b*-qP2VP nanopatterned surfaces, causing the homogenous deposition of multilayers after several bilayers. The root-mean-square end-to-end distance R_E of used PSS and PDDA chains in salt-free aqueous solutions were calculated to be ~40 and ~80 nm, respectively, larger than the size of qP2VP domains. Thus, nanoconfinement was expected for the PSS and PDDA chains upon their adsorption on the qP2VP domains. However, the mass of the polyelectrolyte layer adsorbed on the PS-*b*-qP2VP nanopatterned film was found to be smaller than that obtained on the homogenous qP2VP surface, after multiplication by the surface fraction of qP2VP domains (0.46) (Figure 6E), inconsistent with the finding of Jonas et al.[75] on binary chemically-patterned surfaces, suggesting that the behavior of polyelectrolyte chains adsorbing on nanostripes might need complementary studies to be fully understood.

As for the LbL lift-off approach, a nanopatterned surface was achieved by spin-coating on a substrate an electron-sensitive resist (*e.g.*, poly(methyl methacrylate)), followed by electron beam lithography to create open nano-cavities or stripes in the resist (exposed substrate)[96]. After deposition of LbL multilayers, the nanopatterned resist film was dissolved to fracture the LbL film by the osmotic pressure generated by the concentration gradient resulting from the dissolved polymer resist. As a result, the LbL film was lifted-off at local positions. A key point is the strong interaction between the LbL film and the exposed regions of the substrate, which is crucial to prevent the detachment of the film over the exposed regions. To study the nanoconfinement effect, the width of stripes or diameter of dots should be less or at least comparable to the size of polyelectrolyte coils, typically below 100 nm. However, the reduced contact area leads to unwanted lift-off of the LbL film; therefore, the lowest stripe width that could be successfully fabricated by LbL lift-off was *ca.* 150 nm, well above the average root-mean-square distance between the chain ends of the polyelectrolytes; thus identical film growth was observed on the stripes or dots compared to over the laterally-homogeneous multilayers

(Figure 6G)[91]. Another issue was that when the stripes became extremely narrow, the lifted materials from both sides of the channels merged, resulting in an apparent higher thickness for the LbL assembly and blurring the nanostripes.

It is thus obvious that LbL assembly over nanopatterned surfaces need further efforts to elucidate its full complexity. Here we note that the observed behavior for polyelectrolytes adsorbing on nanostripes is very different from the one reported for polyelectrolytes adsorbing in nanochannels; this suggests that restricted diffusion and coil compression, which only exist in nanochannels, are crucial factors specific to LbL assembly in such nanopores.

4. Applications

The combination of layer-by-layer assembly with nanochannels offers great opportunities to fabricate smart functional nanoobjects and membranes-based devices for various applications. Herein, applications are divided into several categories, depending on whether the functional structures are required to be released or not from the nanoporous membranes.

4.1 Nanochannels as templates to fabricate functional nanotubes/nanorods

Nanochannels were considered as templates for the deposition of LbL films in confined spaces, producing LbL nanotubes/rods after removal of the templates. The most fascinating feature is that the tubular structure has two surfaces (interior and exterior) which can be functionalized independently for performing different tasks.

Typically, membranes with a high density of well-defined nanochannels were employed for the massive production of nano-objects, for instance AAO and ion-track polymer membranes as shown in Figure 1. The polymer PC nanoporous membrane is preferable to the AAO template in the production of LbL nanotubes/rods, because of its more straightforward dissolution in organic solvent, such as CH_2Cl_2 and dimethyl formamide (DMF). The harsher conditions required to etch solid AAO templates (NaOH or H_3PO_4) probably induce deformations in soft LbL tubular structures and may degrade the components incorporated in them.

4.1.1 Collection of liberated nanotubes from membrane templates.

A decrusting step is generally required to remove the LbL crust grown over the porous membranes, so that the dissolution of templates can yield separated nanotubes in solution. The challenge is then the collection of the nanotubes from the solution containing the dissolved template, and their redispersion in a more appropriate medium, typically an aqueous solution which often is a proper environment for practical applications. The simplest way to collect templated nano-objects from suspension is filtration, by which they are collected over a collecting filter and rinsed. However, the critical point of this method is the following transfer of the nano-objects from the filter to an aqueous solution without deformation or rupture. Rubner and coworkers[97] used a cell scraper to rub the filter surface and release the filtration-collected microtubes in aqueous solution. In this case, the short length (5 μm) and sturdy nature of their thick microtubes were key features compatible with this approach; however, this route is hardly applicable to soft LbL-nanotubes of high aspect ratio, which are fragile and strongly sticky[98]. However, filtration[99] and electrophoretic deposition[100] can be employed to collect nanotubes directly from a nanotube suspension over a filter, thereby leading to nanotube mats or biointerfaces on substrates.

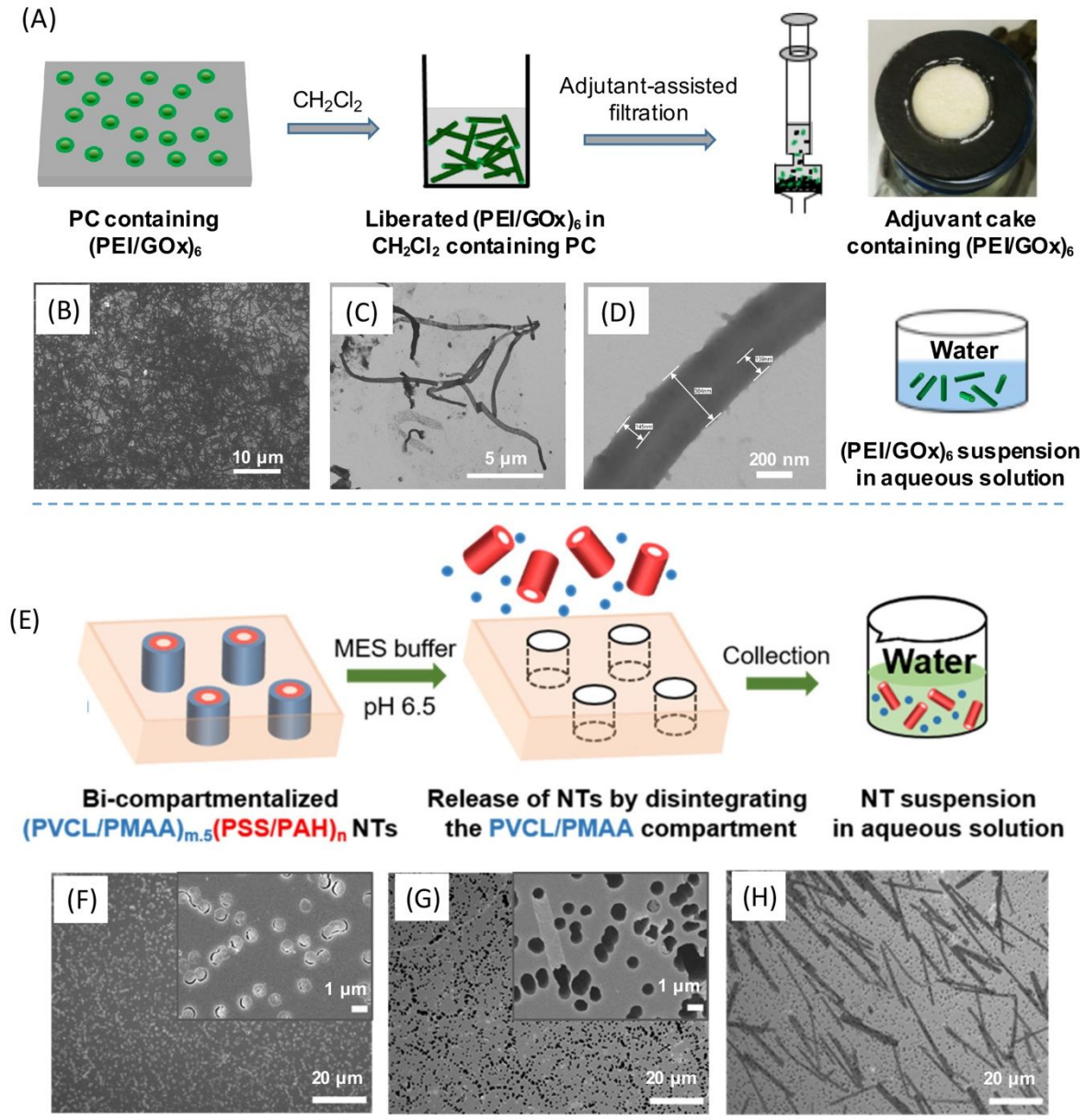

Figure 7. Collection of nanotubes by using (A-D) adjuvant-assisted filtration[85] and (E-H) a sacrificial layer[101]. (A) Schematic illustration of adjuvant-assisted collection. (B) SEM and (C,D) STEM images of liberated $(PEI/GOx)_6$ nanotubes collected from a nanotube suspension in aqueous solution. Adapted with permission from ref. 85. Copyright 2015 American Chemical Society. (E) Schematic illustration of the fabrication of bi-compartmentalized $(PVCL/PMAA)_{m.5}(PSS/PAH)_n$ nanotubes (NTs) and of the release of the inner nanotubes in biologically compatible conditions. (F, G) Top-view SEM images of a membrane filled with (F) $(PVCL/PMAA)_{5.5}/(PSS/PAH)_{12}$ nanotubes and (G) the same after the liberation of fluorescently tagged NTs at pH 6.5. (H) Liberated $(PSS/PAH)_{12}$ nanotubes collected from the resulting nanotube suspension in aqueous solution. $(PSS/PAH)_{12}$ nanotubes were released by

dissolution at pH 6.5 of the sacrificial compartment of bi-compartmentalized $(PVCL/PMAA)_{5.5}/(PSS/PAH)_{12}$ NTs in membranes[101]. Adapted with permission from ref. 101. Copyright 2019 American Chemical Society.

Collection strategies have been developed to transfer liberated nanotubes from template to aqueous solutions. The traditional centrifugation is an effective method to sediment objects in suspension, allowing the purification of nanotubes from a solution containing the dissolved template. When PC membranes are used, the aqueous suspension can be obtained by replacing the pure organic solvent with water when the organic solvent is miscible with water, such as DMF. Large centrifugation forces and long times are, however, required to efficiently sediment nanosized objects. This may provoke the formation of irreversible aggregates. The first achievement of an aqueous suspension of intact nanotubes was reported by Komatsu et al[102]. They used centrifugation to separate the nanotubes from the PC template/DMF solution, resulting in nanotubes suspended in pure DMF, followed by freeze-drying to yield lyophilized nanotubes aligned in a thin film. These resulting pieces of film made of protein nanotubes could be further redispersed in water, leading to a homogeneous but slightly turbid dispersion. Another collection strategy based on adjuvant-assisted filtration (Figure 7A) was developed by Jonas et al[85]. A thin layer of water-soluble adjuvant (for instance, dextran, fructose, NaCl) was first deposited over the filter as buffer layer to prevent the contact of the nanotubes with the filter, followed by co-filtration of a suspension of nanotubes and added adjuvant particles in the polymer/CH_2Cl_2 solution, to form a nanotube-containing adjuvant cake. The resulting cake could be easily detached from the filter and dissolved in water to obtain an aqueous nanotube suspension (Figure 7B-D). These solutions are compatible with biological organisms; for instance, Jonas et al. added commensal skin bacteria to such an aqueous suspension of LbL nanotubes, leading after filtration to bacterial nanofibrillar patches for topical applications.[103]

An alternative strategy does not involve the dissolution of the template. Instead, the nanotubes are released directly from the porous template by disassembly of a sacrificial LbL layer with a proper etching solution. Prior to the assembly of target nanotubes, the sacrificial LbL layer of limited thickness is first built within the nanoporous template. The destruction of this sacrificial LbL layer by flowing through an etching medium to detach the target nanotubes

from the nanochannel walls facilitates the extraction of the nanotubes (Figure 7E). However, this method requires target nanotubes resisting the etching medium (typically, an aqueous solution). Jonas et. al.[101] used hydrogen-bonded poly(methacrylic acid)/poly(N-vinylcaprolactam) (PMAA/PVCL) multilayers as sacrificial layer to release poly(styrenesulfonate)/poly(allylamine hydrochloride) (PSS/PAH) nanotubes (Figure 7E). PMAA/PVCL multilayers are stable at lower pH but disintegrate in a close-to-neutral 0.15 M NaCl aqueous solution, while (PSS/PAH) nanotubes are stable in these biocompatible conditions (Figure 7F-H).

4.1.2 Liberated tubes as micro/nanoreactors

When functional components (e.g. enzymes) are incorporated in LbL assemblies the released nanotubes can act as smart micro/nanoreactors. These functional elements can be used either as both scaffold and active materials, or just as a supplementary functional component inserted in supporting LbL polyelectrolyte tubular structures. For instance, bioactive nanotubes made of only proteins were fabricated in AAO membranes in a layer-by-layer fashion by alternate vacuum filtration of a glucose oxidase (GOx) solution through the membrane, followed by immersion of the membrane in a 0.025% glutaraldehyde (GA) solution.[104] GA has two aldehyde groups which react with the amine groups of proteins to crosslink neighboring protein layers. Moreover, the globular proteins have both amino and carboxylate groups with an isoelectric point (Ip). When the pH of the solution is lower or higher than the protein Ip, proteins carry a net positive or negative surface charge, facilitating LbL assembly with oppositely-charged polyelectrolytes. Jonas el al.[85] used polyethylenimine (PEI) as positive polyelectrolyte to be alternately assembled with GOx to produce enzyme nanotubes. Similarly to pure GOx nanotubes, PEI/GOx nanotubes preserve the bioactivity of GOx. The catalytic activity of liberated PEI/GOx nanotubes toward glucose increases as the number of deposited GOx layer increases, while the embedded nanotube in templates exhibited lower activity, because of the limited access of glucose due to the blocking of pores. Other active protein nanotubes were also reported. Komatsu et al. fabricated many different kinds of protein nanotubes by using GOx[105] or human serum albumin (HSA)[106] assembled with poly(L-arginine) (PLA). Gold nanoparticles (AuNP) display catalytic activity for the reduction of nitrophenols

to amine derivatives in the presence of sodium borohydride ($NaBH_4$), and were also incorporated in PLA/HAS protein nanotubes by co-deposition of HAS and Au nanoparticles[107]. The obtained hybrid $(PLA/AuNP\text{-}HSA)_3$ nanotubes showed higher catalytic efficiency for the 4-nitrophenol (4Nip) reduction than free gold nanoparticles.

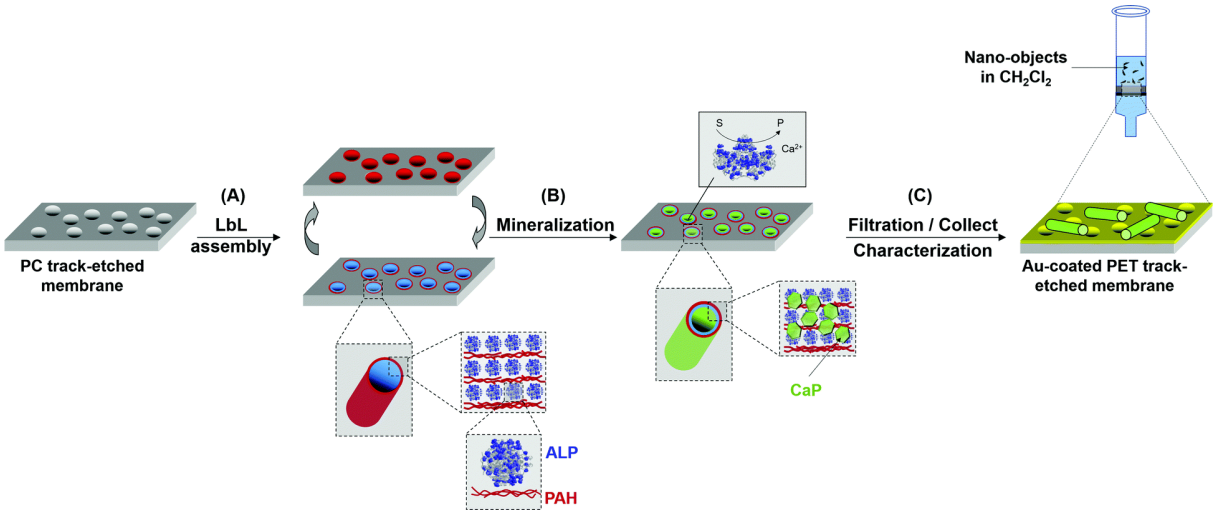

Figure 8. Illustration of the synthesis of mineralized anisotropic calcium phosphate nano-objects by alkaline phosphatase (ALP) immobilized in nanochannels. The ALP nanotubes are capable of hydrolyzing α-glycerol phosphate to generate orthophosphate ions, a calcium phosphate precursor, which leads to calcium phosphate in the presence of Ca^{2+}.[108] Reprinted with permission from ref. 108. Copyright 2020 Royal Society of Chemistry.

Enzymatic reactions occurring in LbL protein nanotubes can also be used to synthesize mineralized nanomaterials. The crystallization process may be controlled by the confinement of LbL nanotubes. Landoulsi and coworkers[108] deposited PAH/ALP multilayer in nanochannels and used immobilized ALP for the local biomimetic production of calcium phosphate (Figure 8). The orthophosphate ions generated by ALP nanotubes allows for in situ nucleation and growth of calcium phosphate particles in the presence of Ca^{2+}. Excitingly, the biomineralization initiated by the immobilized ALP happens in nanoconfined spaces, which leads to the formation of highly crystalline hydroxyapatite.

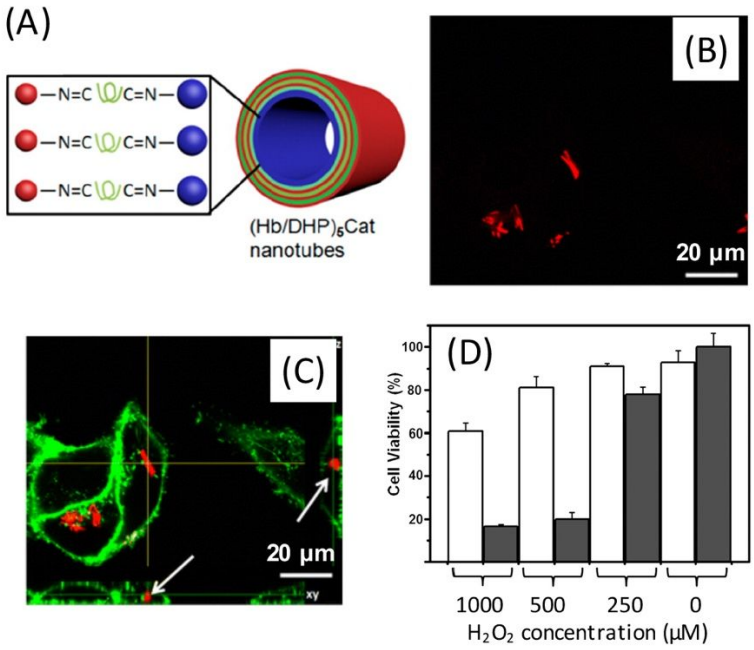

Figure 9. (A) Structure of $(Hb/DHP)_5$Catalase Nanotubes. (B) CLSM images of the autofluorescent $(Hb/DHP)_5$Catalase nanotubes. (C) overlapped image of nanotubes and HepG-2 cells membrane stained with Alexafluoro 488. (D) $(Hb/DHP)_5$Catalase nanotubes improved the viability of HepG-2 cells against oxidative stress.[109] The white column represents the experiment group, and the gray column represents the control group. Adapted with permission from ref. 109. Copyright 2013 American Chemical Society.

Tubular LbL scaffolds can also be first fabricated by using other materials, then followed by the addition of an active component on the inner or exterior surfaces of the scaffolds, depending on needs. Urease was loaded in $(PSS/PAH)_6/(Fe_3O_4/PAH)_2$ nanotubes in a buffer solution at pH 7.2. In this condition, urease is negatively charged and could be easily adsorbed onto the inner PAH layer which is positive. The $(PSS/PAH)_6/(Fe_3O_4/PAH)_2$/Urease nanotubes were used as nanoreactors for the biomimetic synthesis of inorganic materials inside the nanotubes.[110] Li et al.[109] fabricated hemoglobin/dialdehyde heparin $(Hb/DHP)_5$ covalently-bound nanotubes as biocompatible tubular scaffolds for the subsequent deposition of catalase on their inner surface (Figure 9A-C). The assembled hemoglobin nanotubes with catalase interior enzymes possess H_2O_2-scavenging capacity for the protection of cells under oxidative stress (Figure 9D).

Following the same fabrication strategy, tubular nanoreactors modified on their inner wall by GOx[105], *Candida antarctica* lipase B[111] and α-d-glucosidase (αGD)[112] have been demonstrated. By making use of the reactions occurring within the nanotubes, chemical energy could be utilized to propel the nanoreactors. A self-propelled protein microtube motor with a catalase interior surface was reported[113]. Biotinylated catalase biocatalysts were immobilized on the inner wall of $(PLA/HSA)_7PLA/PLG$/Avidin microtubes. In the presence of H_2O_2, the immobilized catalases are capable of decomposing H_2O_2 to produce O_2 bubbles which exit the open-end terminus to propel the microreactors. In the same way, biotinylated ureases (bUre) were anchored on the inner wall of nanotubes to fabricate bubble-free nanomotors (Figure 10A-C). The nanotubes are driven by the consumption of the urea substrate (NH_2CONH_2) in the urease reaction.

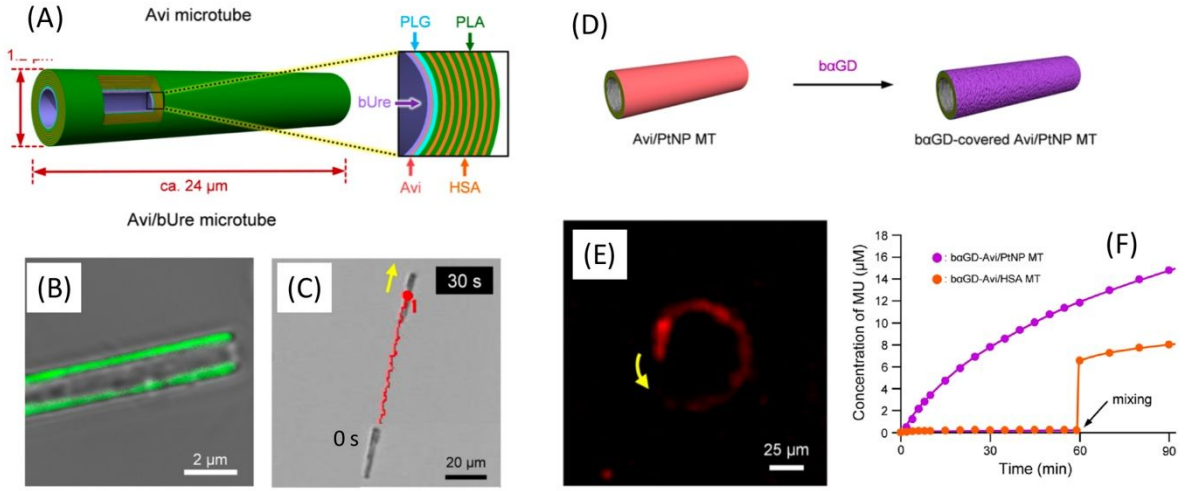

Figure 10. (A) Avidin/biotinylated urease (Avi/bUre) microtube obtained by immobilization of biotinylated urease onto the Avidin interior surface of $(PLA/HAS)_7/PLA/PLG$/Avidin microtubes. (B) CLSM image of Avidin/Fluorescent-biotinylated urease microtube (overlaid image of bright field mode and fluorescence field mode; 488 nm excitation). (C) Motion of self-propelled Avi/bUre microtubes in PB solution (10 mM, pH 6.0) containing 100 mM urea at 25°C.[114] Adapted with permission from ref. 114. Copyright 2019 Wiley-VCH Verlag GmbH & Co. KGaA, Weinheim. (D) Coating of the external surface of $(PLA/HSA)_8PLA/PtNP$ microtubes with α-d-glucosidase (bαGD) active components. (E) Motion of a self-propelled Avidin/PtNP microtube by jetting O_2 bubbles in PB solution (pH 7.0, 1 wt % H_2O_2, 0.2 wt %

Triton X-100) at 25 °C under fluorescence imaging. (F) Activity of α-d-glucosidase (bαGD) externally-immobilized Avi/PtNP microtubes.[115] Reprinted with permission from ref. 115. Copyright 2019 American Chemical Society.

As mentioned before, a tubular structure has two independent surfaces that can be functionalized with different active materials. Figure 10D shows microtubes with Pt nanoparticles (PtNP) on the inner wall, and α-d-glucosidase (αGD) on the external surface[115]. Pt nanoparticles catalyze the decomposition of H_2O_2, producing O_2 bubbles which drive the whole system (Figure 10E) while the external αGD provides the swimmer with biocatalytic activity. It was found that the enzyme reaction occurring at outer surface was improved by the self-propulsive motion, due to enhanced mixing by nanotube-driven stirring (Figure 10F).

Apart from direct functionalization by active components, the activity can also be obtained by post-treatment of LbL nanotubes. For example, photoactive nanoreactors comprising iron oxide nanoparticles were prepared by post-calcination of $(PLA/ferritin)_3$ LbL nanotubes[116, 117]. The resulting Fe_2O_3 nanotubes exhibited higher photocatalytic efficiency than bulk Fe_2O_3.

4.1.3 Liberated tubes for separation

Typically, the separation of targets by micro/nanotubes relies on specific binding between the targets and the functional elements that are incorporated in tube walls or anchored on either inner or external surfaces of LbL nano/microtubes. $(PLA/HSA)_3$ LbL nanotubes have been explored to capture uranyl ions and small molecules (3,3'-diethylthiacarbocyanine iodide, and zinc(II)-protoporphyrin IX) using HSA wall components[102]. The biological function of HSA in the tube was retained and the cylindric wall of $(PLA/HSA)_3$ LbL nanotubes swelled considerably which facilitated the diffusion of target molecules into the wall and specific binding. Moreover, a magnetite (Fe_3O_4) component was incorporated into protein nanotubes to form $Fe_3O_4(PLA/HSA)_3$ magnetite nanotubes which can be easily collected after binding using a magnetic field.[118]

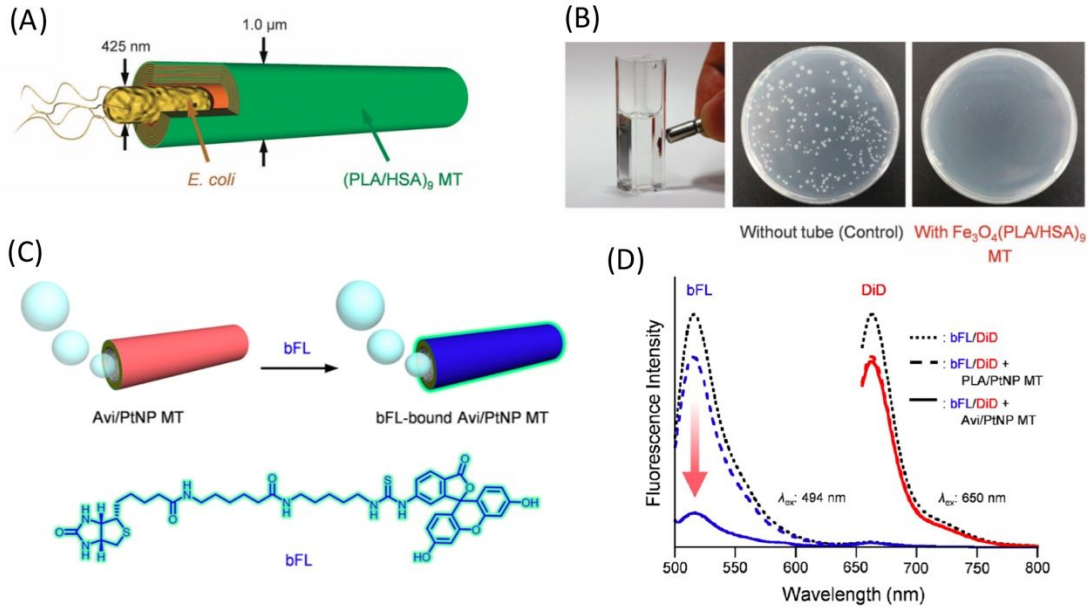

Figure 11. (A) Schematic illustration of *E. coli* entrapped in $(PLA/HSA)_9$ microtubes.[119] (B) Collection of *E. coli*-loaded $Fe_3O_4(PLA/HSA)_9$ MTs by a magnetic field, and appearance of LB agar plates spread with an *E. coli* dispersion previously incubated with $Fe_3O_4(PLA/HSA)_9$ microtubes for 30 min (after 16 h cell culture at 37 ^oC).[119] Adapted with permission from ref. 119. Copyright 2014 Royal Society of Chemistry. (C) Schematic illustration of biotinylated fluorescein (bFL) anchored on the external surface of self-propelled Avidin/PtNP microtubes, based on biotin-avidin interaction[115]. (D) Fluorescence spectra of the PB solution (pH 7.0, 1.0 wt % H_2O_2, 0.2 wt % Triton X-100) of bFL/DiD (λex, 494 nm for bFL; λex, 650 nm for DiD) after treatment with self-propelled Avidin/PtNP microtubes, with subsequent centrifugation[115]. DiD: 1,1′-dioctadecyl-3,3,3′,3′- tetramethylindodicarbocyanine. Adapted with permission from ref. 115. Copyright 2019 American Chemical Society.

For larger objects, such as particles, bacteria or virus, the tubular structure offers ideal spaces for holding them. In this case, the lumen of tubes should have a larger or at least comparable size to targets. For instance, $(PLA/HSA)_2$/PLA/PLG/Avidin nanotubes with 200 nm pore size can selectively allow the selective incorporation and binding of 100 nm biotin-functionalized nanoparticles; thus nanoparticles with different size can be separated.[118] Figure 11A shows a schematic illustration of *E. coli* entrapped in $(PLA/HSA)_9$ microtubes (MTs). These $(PLA/HSA)_9$ microtubes have a hollow structure with an inner diameter of ~700 nm,

larger than the size of *E. coli*. The inner surface HSA layer can bind to *E. coli*. by interacting with expressed surface proteins. The motion of *E. coli*. in response to certain chemicals in the environment was believed to contribute to the *E. coli* capture into the $(PLA/HSA)_9$ microtubes. The use of a magnetic field to collect $Fe_3O_4(PLA/HSA)_9$ MTs after trapping of *E. coli*. clearly is an efficient way for bacteria removal, as evidenced by the absence of bacterial colonies on LB agar plates after MT removal (Figure 11B).[119] Similarly, protein nanotubes functionalized with fetuin[120] or a specific antibody[121] can capture the influenza A virus PR8 (H1N1) or other viruses efficiently.

Similarly to the capture by a properly functionalized inner wall, the external wall can also be utilized for binding of molecules or larger targets. For instance, the positively-charged surface of $PLA/HSA/Fe_3O_4/(PLA/HSA)_5/PLA/Pt$ nanoparticle microtubes was used to electrostatically adsorb negatively charged bacteria (*E. coli*.) (Figure 11C)[122]. Based on the biotin-avidin interactions, biotinylated fluorescein can be captured by avidin on the external wall surface[115]. In the presence of H_2O_2, the capture efficiency was enhanced by the movement of microtubes induced by O_2 bubbles (Figure 11D) (due to the decomposition of H_2O_2 by Pt catalysts anchored on the inner wall).

4.1.4 Liberated tubes for transportation

Cell penetration rather than full internalization of high aspect ratio nanotubes provides an elegant way for transmembrane mass transport, since they can act as an artificial nanochannel through cell membrane.

Abe et al.[123] fabricated poly-L-arginine/poly-L-glutamic acid (PLA/PLG) protein nanotubes by layer-by-layer assembly. The average outer diameter and length of nanotubes were ～400 nm and 5-9 μm, respectively. The internal pore size was larger than 200 nm, which is sufficient to carry any molecule of interest. Studies were performed on the ability of these protein nanotubes to penetrate through HeLa cell membranes, and on the viability of HeLa cells after treatment with protein nanotubes. Results show that most protein nanotubes penetrated into the cell membrane without any major internalization process, and that the cell membrane was intact around the protein nanotubes (Figure 12A). The cells retained their viability after protein nanotube penetration (Figure 12B). Propidium iodide (PI) was observed in the nucleus

of treated cells after 5 min of incubation, indicating the free passage of molecules through protein nanotubes into the cell (Figure 12C). The poration of the cell membrane could be assisted by external stimuli. He et al.[124] constructed a conical $(PSS/PAH)_{10}$ tubular structure by using a template-assisted layer-by-layer technique. The length of the tube was ~10 μm, and the diameters of the two openings were ~200 nm and ~800 nm, respectively, replicating the size of nanoporous templates. The conical tubes exhibited efficient and controllable movement toward target cells like nanoswimmers, through the manipulation of the acoustic field, resulting in attachment of nanoswimmers onto the membrane of HeLa cells with orientation of the small opening. More importantly, Au nanoshells deposited inside the larger opening enabled the poration of the cell membrane within 0.1 s under irradiation by NIR light (Figure 12D). The Au nanoshells on the larger opening convert NIR laser energy into heat and help to penetrate the cell membrane. This was evidenced by the transport of a fluorescent dye through the cell membrane (Figure 12E, F) and by SEM images (Figure 12G).

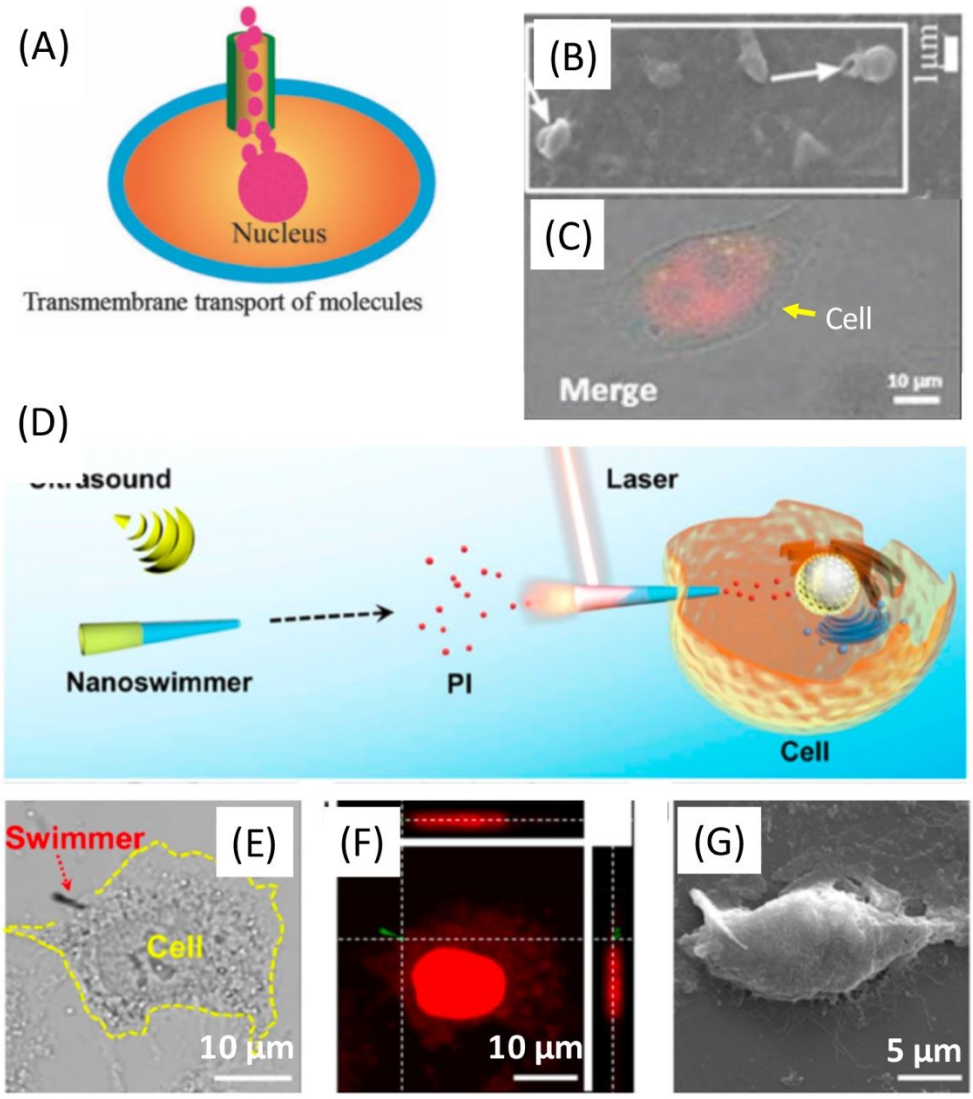

Figure 12. (A) Illustration of transmembrane transport of molecules by nanotubes and (B) SEM image of HeLa cells with penetrated protein nanotubes. White solid arrows indicate the location of protein nanotubes on the cell surface and the white rectangle represents a magnified area of the cell surface with protein nanotubes. (C) CLSM (merge) image of propidium iodide (PI) transported into HeLa cells by nanotubes.[123] Republished with permission from ref. 123. Copyright 2014 Royal Society of Chemistry. Yellow solid arrows show the location of cell .(D) Schematic cell poration of the AuNS-functionalized $(PSS/PAH)_{10}$ nanoswimmers upon exposure to NIR light. (E) CLSM image of the nanoswimmers after cell poration. Yellow dashed line indicates the frontier of the cell. (F) Corresponding 3D CLSM image of (E). (G) SEM image of the nanoswimmer after cell poration.[124] Republished with permission from ref. 124. Copyright 2019 American Chemical Society.

In vivo, kinesins walk along microtubules (polymerization of tubulins) to realize intracellular transport. The integration of motor protein kinesins on LbL tube inner surface is a smart strategy to guide the transport of tubulin microtubes. Upon entering the LbL tubes, the tubulin microtubes walk unidirectionally on the inner surface until they leave the LbL tubes, implying that these LbL tubes are great channel tools for cargo transport[125].

4.1.5 Liberated tubes for drug delivery

Compared to hollow capsules, tubular structures have longer persistence in living systems[17], thus providing interesting carrier platforms for drug delivery. Jonas et. al.[126] investigated the uptake of core/shell nanotube by dendritic cells (Figure 13A). The prepared LbL nanotubes have a rigid $(PAH/PSS)_6$ and a biocompatible protein shell made of Poly-L-ornithine hydrobromide (PLO) and ovalbumin. The successful transport of long protein-loaded robust rigid nanotubes to the cytoplasm of dendritic cells offers the possibility of using them for cargo delivery.

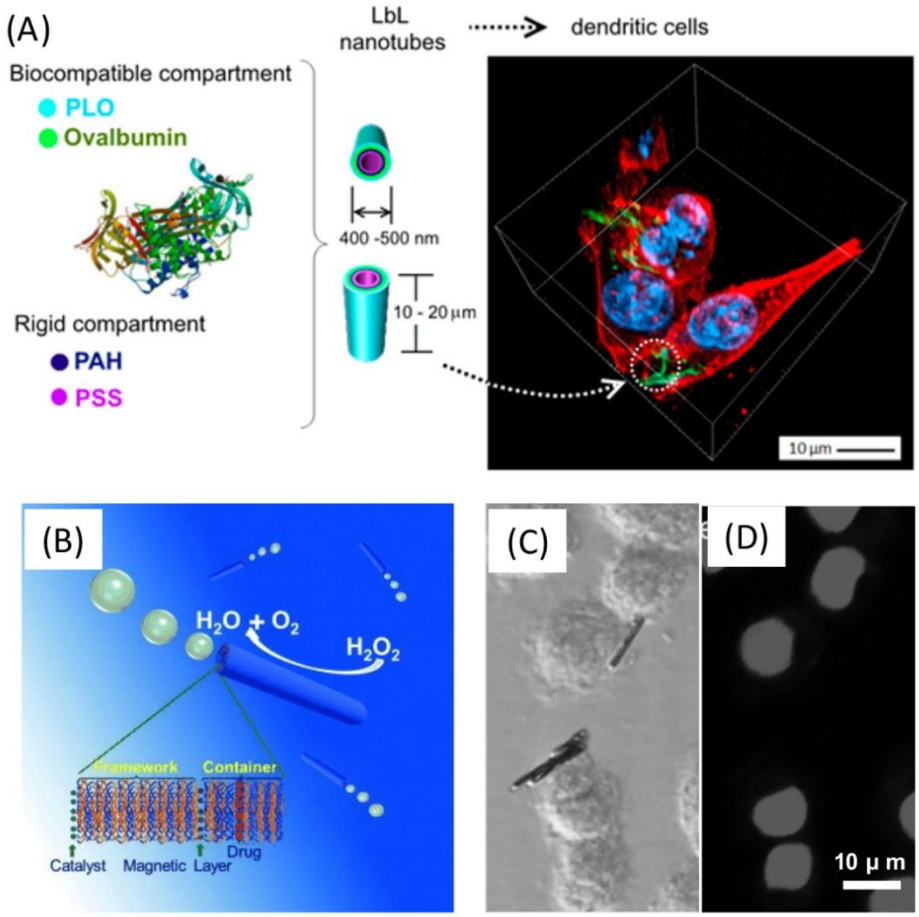

Figure 13. (A) Uptake of long LbL core/shell nanotubes by dendritic cells.[126] Reprinted with permission from ref. 126. Copyright 2017 American Chemical Society. (B) Structure of drug loaded CHI/ALG nanotubes. (C) Differential interference contrast and (C) CLSM images of a $(CHI/ALG)_4$-DOX-$(ALG/CHI)_2$-Fe_3O_4-$(CHI/ALG)_{14}$-PtNP nanorocket after (C, D) treatment with ultrasound in vitro and continuous cultivation of the HeLa cells for 3 h. The incorporated DOX drugs have fluorescent signal. The absence of fluorescent signal from nanotubes indicated the release of DOX drugs from nanotubes. Figures C and D are collected from the same area.[127] Reprinted with permission from ref. 127. Copyright 2013 Wiley-VCH Verlag GmbH & Co. KGaA, Weinheim.

Similarly, the multilayer wall of a LbL-assembled nanotube was designed to have a core/shell structure: the inner layers acting as framework and the outer layers as drug container (Figure 13B)[127]. The nanotubes were made of two biodegradable natural polysaccharides, positively charged chitosan (CHI) and negatively charged sodium alginate (ALG). The cores and shells were separated by a Fe_3O_4 layer and a fluorescent anticancer drug (doxorubicin, DOX) was incorporated in the shell to form a $(CHI/ALG)_4$-DOX-$(ALG/CHI)_2$-Fe_3O_4 layer. Moreover, the inner surface of the core was modified by Pt nanoparticles (PtNP), used to drive the nanorockets by a H_2O_2 fuel (Figure 13B). Under an external magnetic field, the direction of the nanorockets was controlled to approach and finally partially penetrate into the targeted HeLa cells. Then, the DOX drug would be released by destruction of the $(CHI/ALG)_4$-DOX-$(ALG/CHI)_2$-Fe_3O_4 outer multilayer shell with aid of ultrasounds (Figure 13C, D), while the $(CHI/ALG)_{14}$-PtNP inner layer core was found to be robust against ultrasound. It is believed that Fe_3O_4 nanoparticles play a role in disassembly of the drug shell because it is sensitive to ultrasound. In these two examples, drug molecules were incorporated in the LbL nanotube wall. Actually, the inner hollow space is ideal for encapsulation of molecules. The opening of tubes could be capped by silica particle after loading by drug molecules[128]. Biocompatible and responsive materials can be used to construct LbL tube walls which may have tunable permeability by pH or ion strength. For example, when drug-loaded LbL nanotubes reach tumor cells, the more acidic environment may change the permeability of LbL tube wall, allowing the

controlled delivery of drug to target cells. However, until now most attention was paid to LbL capsules[129-131]; no efforts were dedicated to tubular structures.

4.1.6 Liberated microtubes for cancer cell killing

A novel approach was developed to enable cancer cells to be destroyed by the explosion of gold nanoshell (AuNS)-functionalized polymer $(PSS/PAH)_6$ multilayer tubes (Figure 14A).[132] Upon NIR irradiation, the AuNS of the tubes converts light energy into thermal energy. The generated thermal energy causes rapid evaporation of water within the tubes which causes the explosion of the tubes as illustrated in Figure 14A. Prior to NIR irradiation, the tubes were incubated with HeLa cells for 1 h to allow the contact. NIR irradiation caused the tubes to explode into pieces. The destruction of cancer cells stems from the pressure wave-based cell wall rupture, and the piercing of the cancer cells with tube shrapnels as well as thermal damage, since only cells within close proximity of the tubes were destroyed (Figure 14B, C).

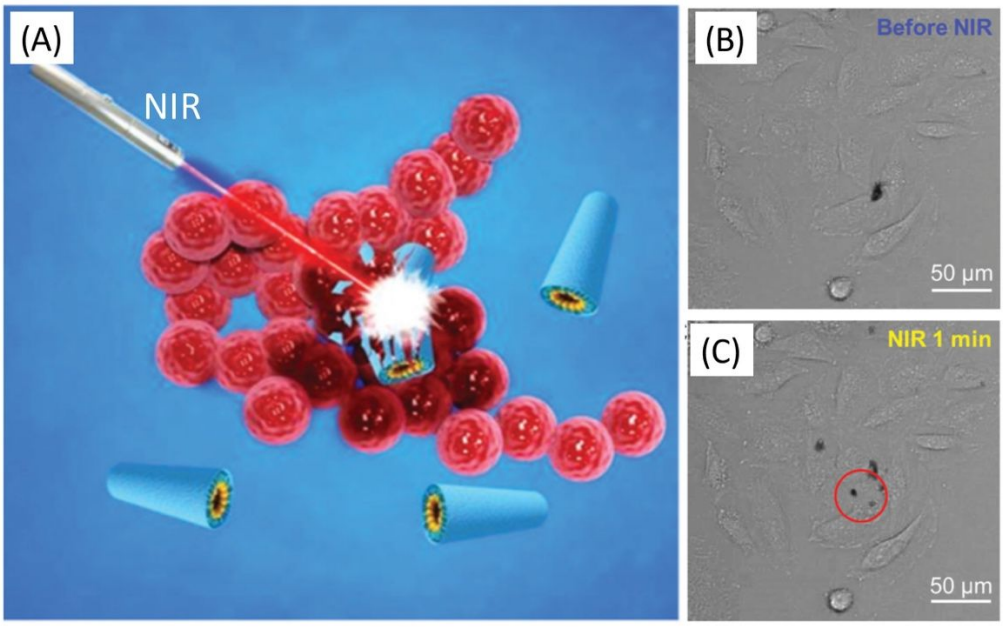

Figure 14. (A) Illustration of NIR-triggered explosion of a tube to kill cancer cells. Bright field microscopy images (B) before and (C) after 1 min laser irradiation of the $(PSS\text{-}PAH)_6$AuNP tube (small gold nanoparticles on the outer surface).[132] Reprinted with permission from ref. 132. Copyright 2015 Wiley-VCH Verlag GmbH & Co. KGaA, Weinheim.

4.2 Channels as templates to fabricate micro/nanotube arrays

Nanopapers made of randomly positioned LbL nanotubes were fabricated by filtration of liberated nanotubes after template dissolution in organic solvent[99, 103]. The nanotubes are then stacked with channels perpendicular to the filtration direction. Alternatively, LbL nanotubes can be arranged in vertical nanotube arrays. Tubular LbL-structures shaped by the nanochannels within templates were anchored onto a support, followed by the removal of the sacrificial templates, yielding nanotube forests. However, due to the distance between the pores in the template, the vertically aligned nanotubes on the supporting substrate have limited contact with their neighboring nanotubes when the template is dissolved, and tend to collapse on the substrate. Consequently, the supporting substrates (typically, porous membranes) are required for most practical applications.

The first example of nanotube arrays was given by Chia who constructed a pH-responsive reversibly swellable $(PAH/PAA)_{20}$ nanotube array by immobilization of PAH/PAA-modified porous PC membranes onto a positively charged glass substrate, via electrostatic interactions[133]. The unattached side of the membrane was then plasma-etched in oxygen to selectively remove the crust film deposited on the membrane surface prior to dissolution in CH_2Cl_2. Protein nanotube arrays immobilized on solid substrates were also proposed by Komatsu[134] as molecular traps in aqueous medium. In that case, crust films on both surfaces of hybrid PC membranes were eliminated prior to nanotube immobilization. The PC membrane containing protein nanotubes was glued onto a cover glass using epoxy resin, which was precoated onto the glass slide, preventing insertion into the nanotubes. Both immobilization approaches lead to the formation of tube brushes.

A promising membrane of LbL nanotubes[135] was achieved for ionic separations following similar protocols. In this work, a PC membrane containing nanotubes was immobilized onto NaOH-treated wet porous polyacrylonitrile (PAN) support upon drying in an oven at 80 °C rather than using glue, before being immersed in CH_2Cl_2 to dissolve the PC framework (Figure 15A). Then, the authors went a step further by depositing another type of functional nanotubes onto the first prepared nanotube array, followed by the formation of a sealing layer on top of the mixed nanotubes (Figure 15B). Interestingly, the sequential deposition of nanotubes leads to well-arranged tubular elements without overlap, producing a densely-packed mixed

nanotube array. The mixed nanotube brushes exhibit higher ion rejection than other types and are capable of enriching in NaCl a solution that permeates through the membrane (Figure 15C).

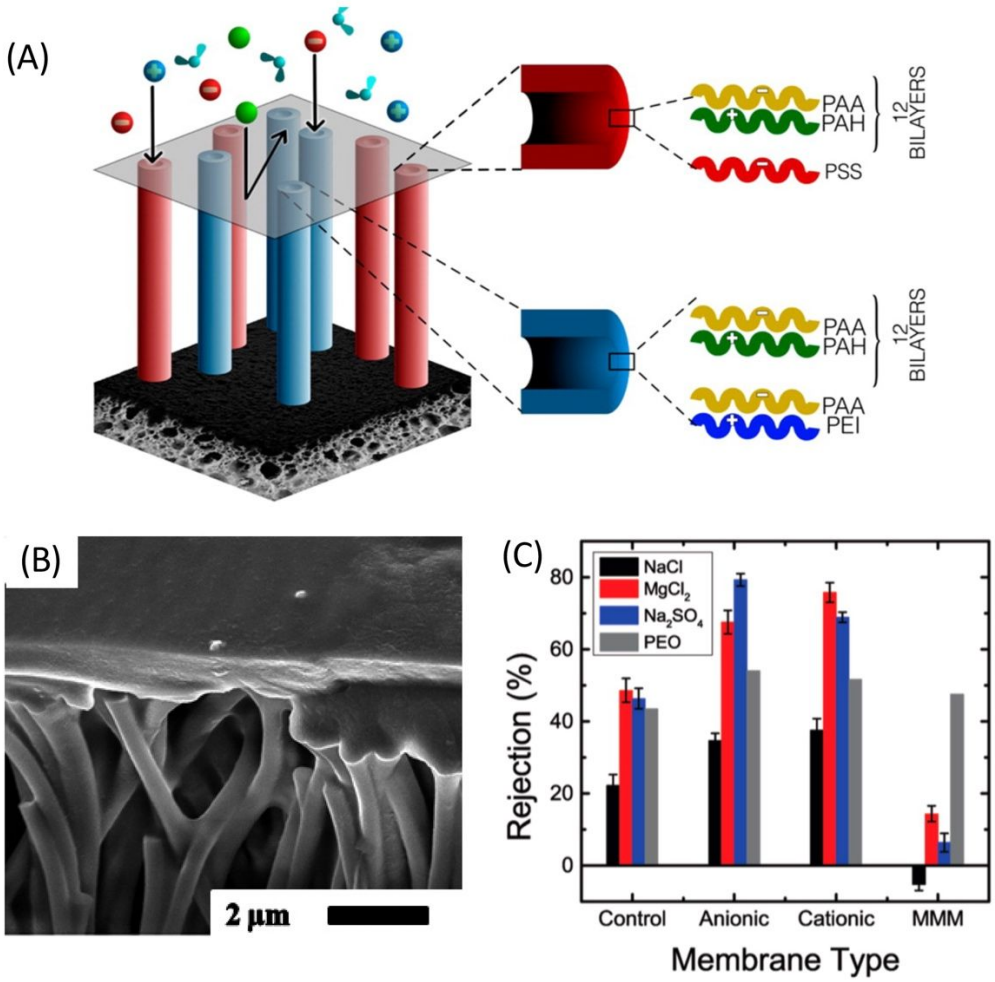

Figure 15. (A) Schematic of the mixed mosaic membranes (MMMs) prepared using LbL assembly. Cationic (blue) and anionic (red) nanotubes are aligned vertically on a support membrane, and a sealing layer is applied to prevent convective flow through the interstitial regions between the nanotubes. Dissolved ions (blue and red spheres) can permeate through nanotubes lined by moieties with the opposite charge, which results in higher ionic permeabilities compared to the permeability of neutral molecules (green spheres). (B) SEM image of formed MMM with the sealing layer on top of the PEI-terminated and PSS-terminated nanotubes. (C) Comparison of solute rejection for charged and neutral solutes between four different membranes. The control membrane was made by depositing the sealing layer (i.e., 3.5 bilayers of PAH and PAA) directly onto the support membrane, anionic membranes were produced by functionalizing the support with PSS-terminated nanotubes then applying the

sealing layer, cationic membranes were produced by functionalizing the support with PEI-terminated nanotubes then depositing the sealing layer, and the MMMs were produced by functionalizing the PAN support with both PEI-terminated and PSS-terminated nanotubes before applying the sealing layer.[135] Reprinted with permission from ref. 135. Copyright 2014 American Chemical Society.

Recently, a light harvesting system was constructed by using PAH/PSS LbL microtube arrays in which the inner space was used as container for a sol-gel solution with an incorporated chloroplast photosystem (PSII) (Figure 16A); this system is analogous to the light absorption organ of plant leaves which have a palisade-like tissue consisting of cylindrical cells aligned perpendicular to the epidermis. The mixture containing PSII was injected into the polyelectrolyte-modified PC membrane, followed by selectively removing the PC template using dichloromethane, resulting in a PSII-based sandwich-like scaffold with well-defined hierarchical structure (Figure 16B, C). The photochemical conversion activity of the hierarchical light-harvesting architectures was evaluated by investigating the production of ATP.

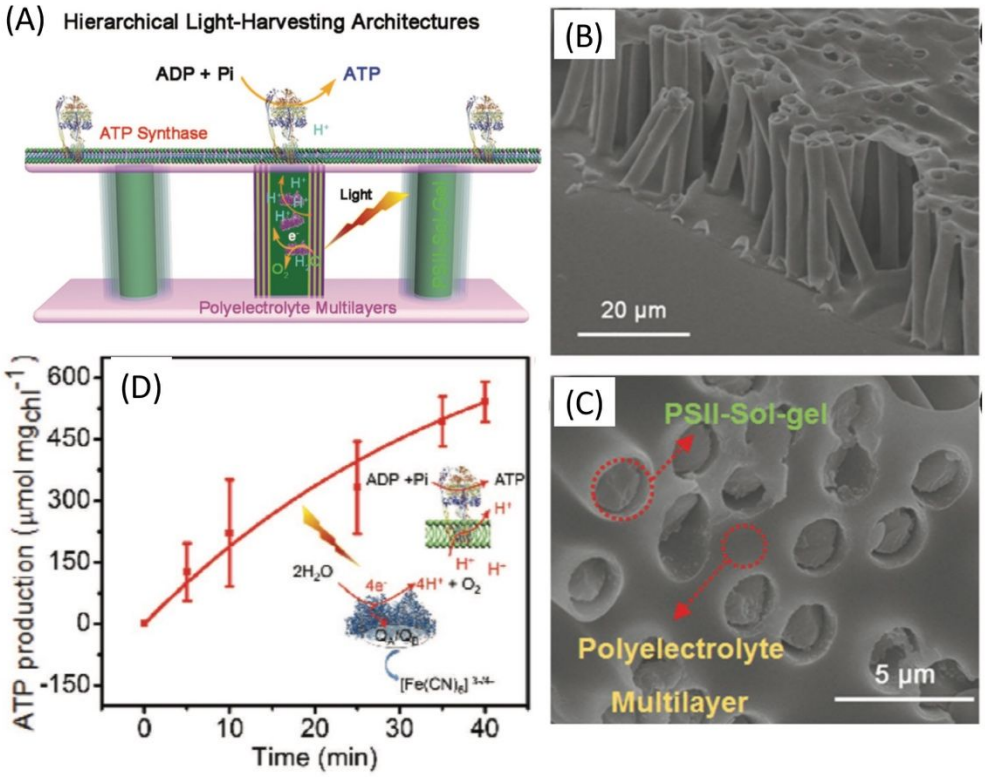

Figure 16. (A) Schematic representation of a bioinspired system capable of photophosphorylation. In this biomimetic system, the polyelectrolyte multilayered membrane serves as the scaffold, resembling the shell of a cylindrical cell in natural plant leaves. The photophosphorylation units, PSII and ATP synthase, are compartmentalized in the silica sol-gel inside the polyelectrolyte microtubes. PAH, poly(allylamine hydrochloride); PSS, poly(sodium-p-styrenesulfonate); PSII, photosystem II; Pi, inorganic phosphate. ATP, adenosine triphosphate; ADP, adenosine diphosphate. The lipid bilayer is composed of dimyristoylphosphatidylcholine (DMPC) (green) and dimyristoylphosphatidylglycerols (DMPG) (purple). (B) Cross-section and (C) top view of the modified polyelectrolyte microtube array. (D) Photophosphorylation assay of the hierarchical light-harvesting architectures.[136] Reprinted with permission from ref. 136. Copyright 2018 Wiley-VCH Verlag GmbH & Co. KGaA, Weinheim.

Under light illumination, PSII in such a highly ordered light-harvesting array, splits water to produce oxygen, protons and electrons; the electrons are captured by an electron acceptor, while the protons are accumulated to promote the rotational catalysis of ATP synthase spreading on the surface of the membrane to produce ATP (Figure 16D). The production rate of ATP production in this hierarchical light-harvesting architecture is enhanced 14 times, compared to that in nature, showing great potentials for artificial energy harvesting devices.

4.3 Channels as membrane scaffolds for functional multilayers

In this case, the nanochannel membranes are used as the supporting scaffolds for the functional LbL layer for various tasks[137], for instance water purification[138, 139], ion separation/selectivity/gating[140-144], nanofluidic diode[145], molecule separation[140], biosensing[146-148] and energy harvesting[149].

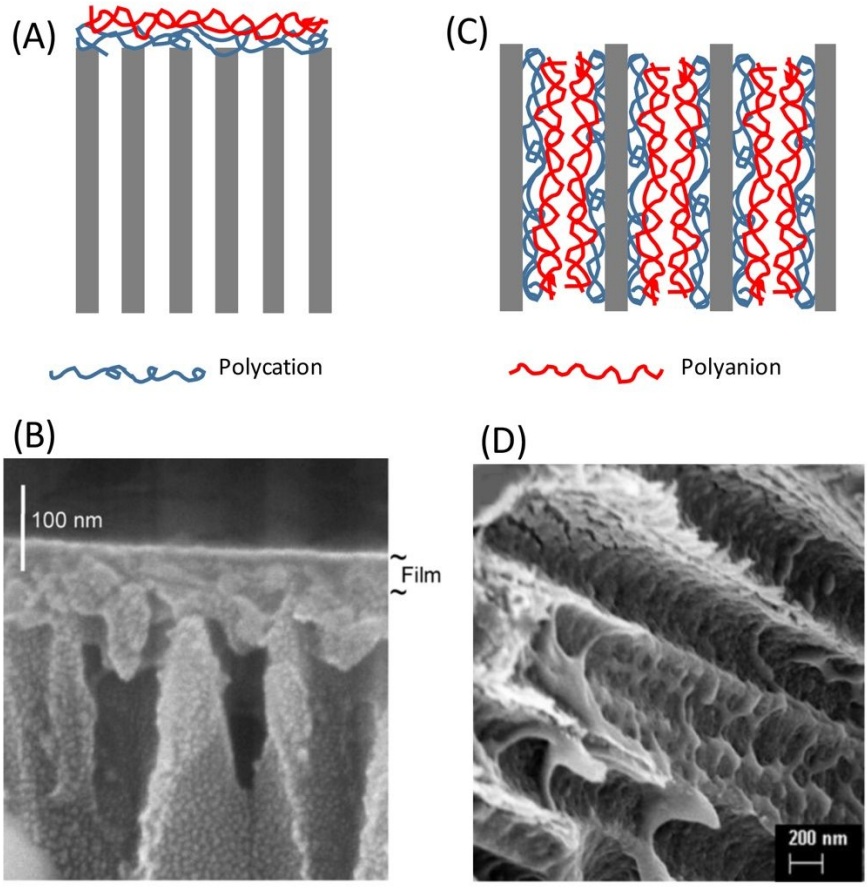

Figure 17. Two configurations of LbL modified nanochannel membranes. Functional membranes prepared by the deposition of a polyelectrolyte multilayer film (A, B) on a support with small pores and (C, D) in large nanochannels. (B) $(PSS/PAH)_5$ film on 20 nm pore size AAO membrane[150] (Reprinted with permission from ref. 150. Copyright 2008 Elsevier); (D) $PEI/(PSS/PDDA)_{15}$ in 400 nm diameter PET nanochannels[151] (Reprinted with permission from ref. 151. Copyright 2013 Elsevier). PDDA: Poly(diallyldimethylammonium chloride).

In fact, when a nanoporous membrane is alternatively immersed in the polyelectrolyte solutions, assembly takes place both on the nanochannel inner surface and on the outer surface of the membrane. After the pore is filled by a polyelectrolyte film, assembly would still happen on the surface to allow film growth. When the film on the surface becomes thick enough, it will gradually dominate the chemical/physical properties of the functional membranes[152]. Small pore size would strongly limit the diffusion of polyelectrolyte chains to the nanochannels, thus the multilayer film is mainly formed on the surface of membrane (Figure 17A). Figure 17B shows the LbL film formed only on the surface of an AAO membrane with 20 nm pore size.

This functional membrane exhibits 95% rejection of $MgCl_2$ along with a Na^+/Mg^{2+} selectivity of 22, as a result of the functional surface LbL film[150]. For larger pores, the main contribution comes from the LbL films assembled on the inner channel surfaces (Figure 17C). The presence of a LbL film was observed in nanochannels of 400 nm diameter (Figure 17D)[151]. Actually, the outer surface LbL film is often preferred for applications, for instance for water purification[153-163], ion[164-173] or molecule separation[174, 175], gas separation[176-179], element recovery[180, 181], and anti-fouling[182-189]. However, in this review, we only focus on LbL assemblies in nanochannels, thus applications mainly based on the functionality of LbL multilayer films resting over the nanoporous membrane surface will not be reviewed here.

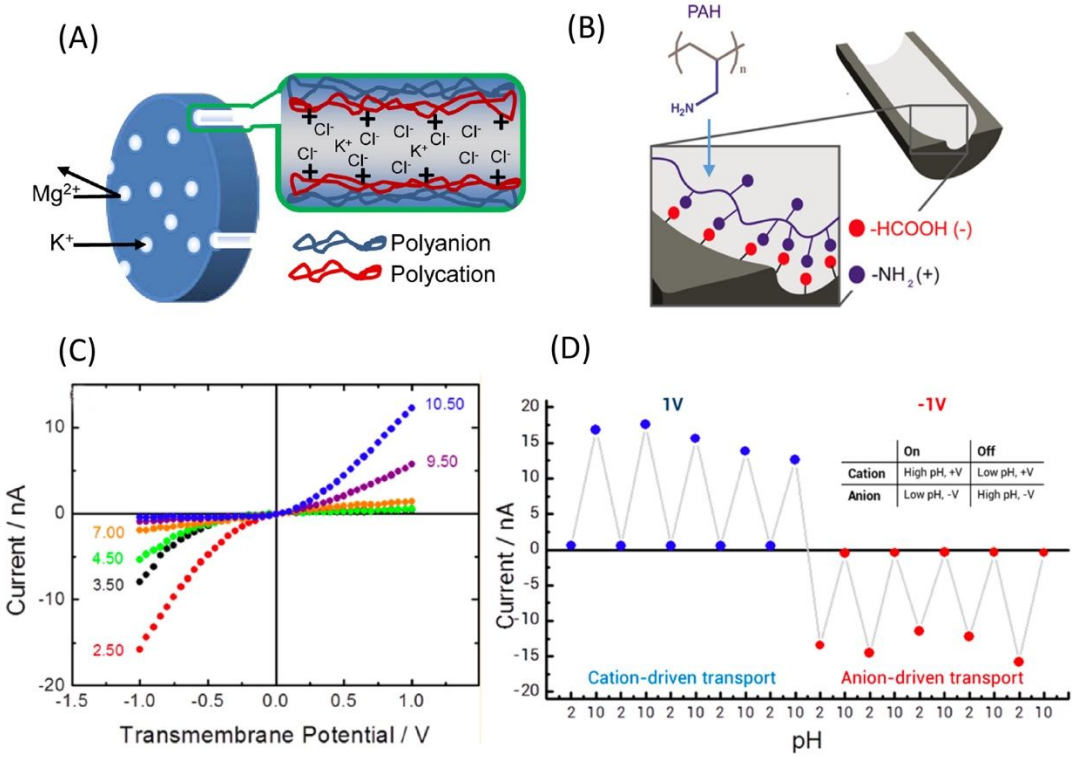

Figure 18. Porous membranes with internal LbL modification for (A) ion separation[190] (Reprinted with permission from ref. 190. Copyright 2013 American Chemical Society) and (B-D) ion rectification and gating[143] (Reprinted with permission from ref. 143. Copyright 2017 American Chemical Society).

For ion selective separation, the blocking of pores by an outer surface LbL film is preferred, because it increases ion selectivity[152]. However, the filling of pores can also increase the resistance of membrane systems, resulting in a limited ion flow. Bruening et al. [190] investigated

the ion separation property of track-etched membranes modified by different numbers of PSS/PAH bilayers (Figure 18A). For nominal 50 nm pores modified with $(PSS/PAH)_4$, the pore size decreased to *ca.* 15 nm, regardless of the ionic strength of the rinse medium, indicating that a LbL film was built in the nanochannels. Results show that K^+/Mg^{2+} selectivity increases to values as high as ~8 after deposition of $(PSS/PAH)_2$ and $(PSS/PAH)_3$ films ending by a positive charge, but then decreases for membranes containing $(PSS/PAH)_4$ coatings. Changing the rinsing solution during polyelectrolyte deposition from water to 0.5 M NaCl leads to a small increase in selectivity, perhaps because rinsing with the salt solution decreases the swelling of the outer PAH layer, implying that the LbL film structure is significant for ion selectivity. When a conical nanochannel was used, the intrinsic rectification was enhanced by introduction of surface charges. As shown in Figure 18B, PAH chains were adsorbed onto the inner negative surface of a single conical nanochannel to create a fluidic diode which selectively transports counterions (ion gating); this selectivity results from the electrostatic interaction between the charged pore surface and the ions passing through them under an electric field across the nanochannel membrane[191]. The PAH modified nanochannel exhibits pH-dependent rectifying behavior because the net surface charge of the nanochannel is sensitive to pH (Figure 18C). The (de)protonation of amine groups along PAH chains and carboxylate groups of the PET pore wall underneath the PAH layer accounts for this pH responsiveness. Actually, in asymmetric nanochannels, the flow of ions occurs preferential from the tip side (narrower opening) to the base side (larger opening)[34]. In acidic solutions, the positive surface charges make the nanochannel anion-selective; this facilitates anion transport from tip to base, driven by a negative voltage bias (working electrode placed at the tip side), resulting in a large anionic current (On state, Figure 18D). The limited anion flow from base to tip and cation flow from tip to base produces a small ion current under a positive voltage bias (Off state). When in alkaline solution, the cation ions become major current carriers because of the reversed surface charges of the now positively charged nanochannel. The current-voltage curves are reversed as well, with large/small ion currents at positive/negative voltage biases (Figure 18C, D).

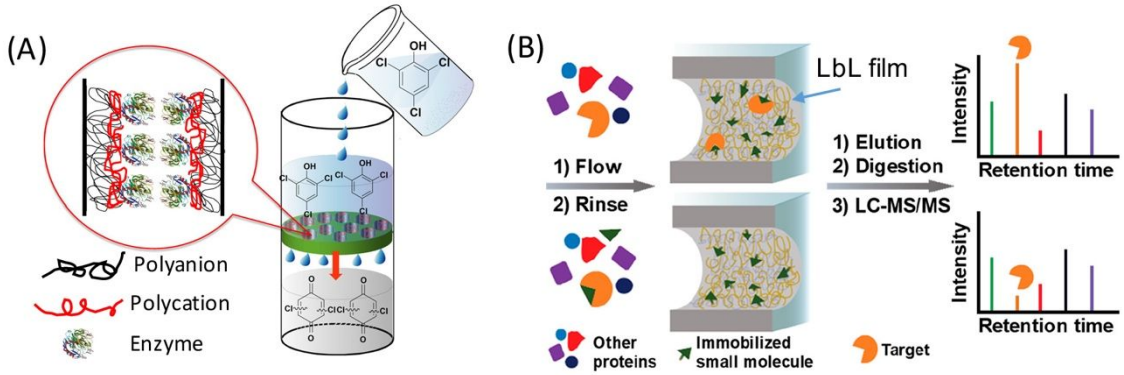

Figure 19. Porous membranes with internal LbL modification for (A) catalysis[192] (Reprinted with permission from ref. 192. Copyright 2017 American Chemical Society), and (B) target protein binding and identification[193] (Reprinted with permission from ref. 193. Copyright 2020 American Chemical Society).

Likely, functional components could be integrated into membranes to create catalytic platforms[192] as shown in Figure 19A. PAA/PAH/Laccase was built in PVDF microfiltration membranes with average pore diameter of 200 nm[192], leading to a decrease of average pore diameter to ~70 nm. The unfilled space with nanotubes facilitates the access of substrate to the inner layer of enzymes. Under a pressure-driven continuous flow mode, over 80% of the initial 2,4,6-trichlorophenol (TCP) was dechlorinated at an optimum flow rate under an applied air pressure of about 0.7 bar or lower which gives a residence time of only 36 s, whereas it takes hours for degradation in a batch reaction. GOx was also electrostatically immobilized with alternative adsorption of PLL in pores of 450 nm diameter within nylon microfiltration membranes, for the catalytic oxidation of glucose[194]. The immobilized GOx has a higher stability against a wide range of pH than free GOx. Besides bioactive enzymes, gold nanoparticles were electrostatically incorporated in the channels. A high density of well-distributed nanoparticles in the membrane pores was achieved[195, 196], capable of selectively catalyzing the reduction of nitro groups in compounds containing other reducible functionalities such as cyano, chloro, and styrenyl moieties. When an antibody was adsorbed on the oppositely charged polyelectrolyte layer, the functional membranes become biosensing platforms based on antibody-antigen specific interactions[197]. Recently, a waveguide spectroscopy strategy was developed to sense the binding events between a small target and anchored receptors

immobilized in nanochannels[198]. This technology employs optical signals, thus do not require labelling of small analytes. Benefiting from the large internal surface area of nanoporous membranes, the binding of a minute quantity of unlabeled material over the pore inner surfaces may produce a significant change in the overall optical density and hence a detectable signal.

Functional molecules can also be covalently anchored to the LbL film by crosslinking chemistry. For example, post-modifications by an antibody[199] and DNA[200] were conducted for the detection of target molecules. Bruening et al.[193] went further to elute proteins for mass spectrometry (MS) to identify the target protein of immobilized small molecules. As shown in Figure 19B, they fabricated PAA/PEI/PAA layers in porous nylon membranes, followed by the immobilization of 4-(2-aminoethyl)benzenesulfonamide (AEBSA) using EDC/NHS chemistry. Carbonic anhydrase II (CAII) was used as the target protein to bind to immobilized AEBSA to examine the efficiency and selectivity of affinity capture in AEBSA modified membranes. Subsequent selective elution of captured proteins and tryptic digestion for MS analysis identified CAII as the dominant AEBSA target in diluted serum or cell lysate.

Based on single conical nanochannels, ion transport properties (ion selectivity, gating and rectification) could be used to detect target molecules. Figure 20A shows the layer-by-layer assembly of biotinylated poly(allylamine) (b-PAH)/streptavidin in single conical nanochannels based on the biotin-avidin specific interactions. The biotinylated poly(allylamine) has bifunctional groups which are able to electrostatically interact with the negative nanochannel surface and expose the binding sites (biotin) for biorecognition of streptavidin proteins. Both adsorption and biorecognition can be transducted in an electronic signal provided by the ionic flux through the pore. The b-PAH-modified single nanochannel are characterized by diode-like current-voltage (I-V) curve with a large rectified ion current at negative voltage bias. The presence of streptavidin at even 1 pM leads to a dramatic decrease in rectified current at negative voltage biases due to the blockade of the nanochannel and its decreased surface charge density. This effect was even more pronounced when more concentrated streptavidin solutions were employed (Figure 20B). Formation of (b-PAH/streptavidin)$_2$ in the nanochannel led to an almost complete blockade of the nanopore (Figure 20C).

Enzymatic reactions could also be utilized to detect an enzyme substrate in a nanochannel when the products can interact with the inner surface of the nanochannel and alter its

chemical/physical properties; thus this may induce a detectable change in ion current. In this case, the single nanochannel can act as a biosensor. Following this principle, a urea sensor was designed by using a PAH/urease modified conical nanochannel (Figure 20D)[148]. The electrostatically immobilized urease catalyzes the decomposition of urea into ammonium and carbonic acid. The byproduct OH^- increases the local pH inside the nanochannel which inevitably changes the surface charge density and even polarity. The charges on the inner surface of the conical nanochannel determine the rectification behavior[201], thus the urea concentration can be correlated to the rectification behavior which is characterized by a rectification efficiency ($|I_{1V}/I_{-1V}|$) (Figure 20E). The smaller the surface positive charge density, the weaker the extent of rectification.

Mesopores are ideal candidates for osmotic energy harvesting under salt gradient because of the large ion flux through mesopore membranes.[202, 203] However, the high ion selectivity is typically difficult to achieve for mesopores because of the limited overlap of electric double layers in mesopores. Therefore, a highly charged surface of confined mesopores is required to induce mesopore rectification which offers preferential and amplified ion transport to promote the osmotic energy efficiency[204, 205]. A highly charged polyelectrolyte, poly-L-lysine, was deposited in the tip opening (>400 nm) to create a mesopore rectifier[149] serving as anion-selective pore system as shown in Figure 20F. Under a salt concentration gradient, anions were selectively transported from high concentration to low concentration, producing osmotic power (Figure 20G). As shown in Figure 20H, the power density (W/m^2) increased as the salt gradient became larger and reached *ca.* 1000 W/m^2 when a 500/1 configuration was applied. These polyelectrolyte modified single mesopore systems are thus promising platforms for harvesting energy from seawater.

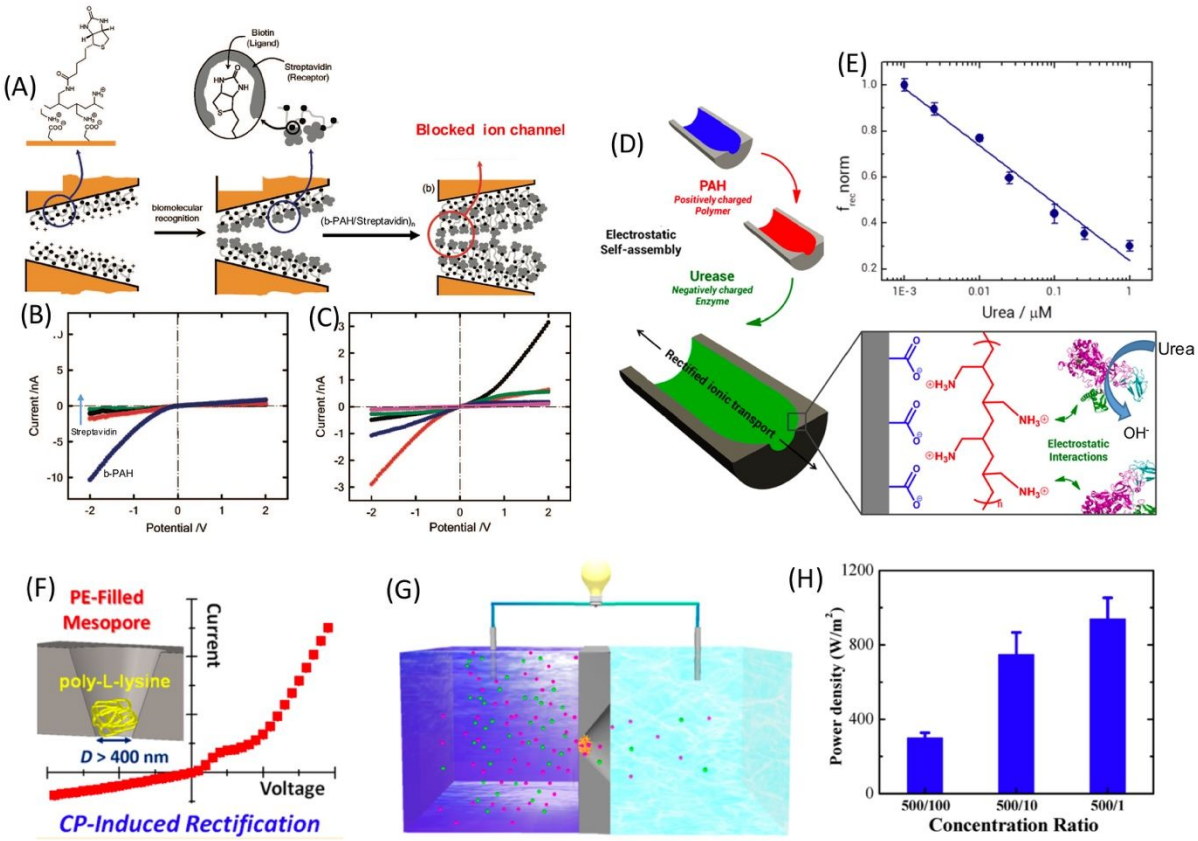

Figure 20. Single conical nanochannel-based systems fabricated by layer-by-layer assembled (A) biotinylated poly(allylamine) (b-PAH)/streptavidin[147], (D) PAH/urease[148] and (F) deposition of poly-L-lysine[149]. (B) Current-voltage characteristics of a biotinylated poly(allylamine) (b-PAH)-modified single conical nanopore in 0.1 KCl in the presence of different concentrations of streptavidin (SAv): (dark blue) no streptavidin; (red) 1 pM; (black) 10 pM; (green) 100 pM. (C) Current-voltage characteristics of a surface-modified single conical nanopore in 0.1 M KCl corresponding to (black) carboxylate-terminated pore; (red) b-PAH modified pore; (green) b-PAH/streptavidin modified pore; (dark blue) (b-PAH/streptavidin/b-PAH) modified pore; (pink) (b-PAH/ streptavidin)$_2$ modified pore. Reprinted with permission from ref. 147. Copyright 2008 American Chemical Society. (E) Normalized rectification efficiencies versus urea concentration obtained from the I-V curves recorded after treatment by different concentrations of urea. Rectification efficiency: $|I_{1V}/I_{-1V}|$. Reprinted with permission from ref. 148. Copyright 2018 American Chemical Society. (F) Concentration polarization (CP) induced rectification of poly-L-lysine filled mesopores. (G) Schematic of the system under salt gradient; 500 mM KCl was placed on the side of the membrane with a narrow opening of ~400 nm, while the other side of the membrane was in contact with 1, 10, or 100 mM KCl. (H)

Osmotic power density of poly-L-lysine filled mesopore as a function of KCl concentration gradient. Reprinted with permission from ref. 149. Copyright 2019 American Chemical Society.

When the LbL film was deposited in the nanochannels, the formation of LbL film on the surface of the membrane was inevitable. In membrane-based platforms where applications rely on the functional elements in/on LbL films confined in the nanochannels, the nanoscale LbL film on the surface of membrane has limited contribution. However, these "useless" LbL nanofilms on the surface of membranes can be designed to be anti-biofouling[151], reducing nonspecific binding[199]; this helps improve both the sensitivity and selectivity of membrane-based sensors. For example, antibodies were covalently anchored on the pre-deposited LbL film in nanochannels for effective antigen analysis, while the PAA terminated-LbL film deposited on the surface of AAO membrane provided resistance to protein adsorption in media with physiological salt concentrations of ~0.15 M, facilitating the detection of proteins at subnanogram-per-mL levels in complex matrixes, such as diluted plasma[199].

5. Conclusions

Here, LbL assembly in nanochannels was reviewed with respect to building materials, supporting nanochannels, film growth mechanism, film structure and related applications. In particular, the peculiarity of assembly in confined nanochannels was demonstrated, showing the different assembly mechanism compared to that on "open" flat substrates. As the film grows in nanochannels, the pore becomes smaller, resulting in an enhanced confinement. The polyelectrolyte chains would present an elongated conformation to some extent, leading to a slower growth. Based on the diversity of available building materials, functional tubular LbL assemblies could be employed either as liberated nanotubes/nanorods or in the nanochannels of a membrane, depending on the requirements of applications. Applications were summarized for liberated nanoassemblies, nanotube arrays and tube-functionalized membranes. After collection and transfer of liberated nanotubes from the nanochannel template to an appropriate medium (typically, an aqueous solution), they could be used as nanoreactors, transporters, drug carriers and even cancer cell killers, because these separated nanotubes are capable of penetrating the cell membrane or being internalized by cells. Robust nanochannel membranes are ideal scaffolds for functional nanotubes arrays for ion separation and other fluidic

membrane-based platforms. Notably, the substrate is not limited to the nanochannels that were summarized in this review, revealing the general applicability of LbL assembly to create various useful nanomaterials.

Although LbL assembly is certainly promising to create diverse functional materials, it has some drawbacks as well: slowness of the fabrication process, difficulty to liberate the nanostructures from the supporting substrates in gentle conditions, low mechanical strength of pristine polyelectrolyte LbL nanofilms, and possible structural reorganization of the soft walls of the nanostructures when liberated in solution, to cite the main ones. However, the good compatibility of LbL technology with crossover technologies from other fields offers smart strategies to solve some issues. Automation in a continuous roll process could for instance improve the production rate. By incorporating suitable functional groups (*e.g.*, photocross-linkable azide groups) into building blocks, photo-crosslinking could be employed, providing a robust way to control the placement of functional segments and stabilize the templated nanostructures as well.[206] Crosslinked LbL structures are typically robust enough to be self-supporting, and display hindered internal chain mobility which is needed for long-term stability. There is thus still a large space to be exploited to make further progress in LbL assembly. Beyond applications summarized here, we thus hope that this review will contribute inspiring other researchers to extend further this technology to new fields for performing useful tasks.

Acknowledgements

This work was financially supported by the China Postdoctoral Science Foundation (2020M672437), and Postdoctoral Innovation program of Hubei Province (2020035026). This work was also supported by the Belgian Science Policy (IAP P6/27), and the Belgian Fund for Scientific Research (FNRS).

References

1. J. J. Richardson, M. Bjornmalm and F. Caruso, *Science*, 2015, **348**, aaa2491.
2. J. A. Zasadzinski, R. Viswanathan, L. Madsen, J. Garnaes and D. K. Schwartz, *Science*, 1994, **263**, 1726-1733.
3. J. E. Greene, *J. Vac. Sci. Technol. A*, 2017, **35**, 05c204.
4. F. C. Walsh and C. Ponce de Leon, *Trans. IMF*, 2014, **92**, 83-98.
5. A. Ulman, *Chem. Rev.*, 1996, **96**, 1533-1554.
6. A. Calvo, B. Yameen, F. J. Williams, G. J. Soler-Illia and O. Azzaroni, *J. Am. Chem. Soc.*, 2009, **131**, 10866-10868.
7. B. Yameen, M. Ali, R. Neumann, W. Ensinger, W. Knoll and O. Azzaroni, *Chem. Commun.*, 2010, **46**, 1908-1910.
8. B. Yameen, M. Ali, M. Álvarez, R. Neumann, W. Ensinger, W. Knoll and O. Azzaroni, *Polym. Chem.*, 2010, **1**, 183-192.
9. B. Yameen, M. Ali, R. Neumann, W. Ensinger, W. Knoll and O. Azzaroni, *Nano Lett.*, 2009, **9**, 2788-2793.
10. B. Yameen, M. Ali, R. Neumann, W. Ensinger, W. Knoll and O. Azzaroni, *J. Am. Chem. Soc.*, 2009, **131**, 2070-2071.
11. A. Calvo, B. Yameen, F. J. Williams, O. Azzaroni and G. J. Soler-Illia, *Chem. Commun.*, 2009, DOI: 10.1039/b822489g, 2553-2555.
12. Z. Yang, S. Zhang, V. V. Tarabara and M. L. Bruening, *Macromolecules*, 2018, **51**, 1161-1171.
13. R. K. Iler, *J. Colloid Interface Sci.*, 1966, **21**, 569-594.
14. G. Decher and J.-D. Hong, *Makromol. Chem., Macromol. Symp.*, 1991, **46**, 321-327.

15. G. Decher and J. D. Hong, *Ber. Bunsenges. Phys. Chem.*, 1991, **95**, 1430-1434.

16. P. Bertrand, A. Jonas, A. Laschewsky and R. Legras, *Macromol. Rapid Commun.*, 2000, **21**, 319-348.

17. T. Komatsu, *Chem. Lett.*, 2020, **49**, 1245-1255.

18. C. J. Roy, C. Dupont-Gillain, S. Demoustier-Champagne, A. M. Jonas and J. Landoulsi, *Langmuir*, 2010, **26**, 3350-3355.

19. G. Perez-Mitta, M. E. Toimil-Molares, C. Trautmann, W. A. Marmisolle and O. Azzaroni, *Adv. Mater.*, 2019, **31**, e1901483.

20. P. Apel, *Radiat. Meas.*, 2001, **34**, 559-566.

21. J. Zhang, J. E. Kielbasa and D. L. Carroll, *Mater. Chem. Phys.*, 2010, **122**, 295-300.

22. K. Xiao, Y. Zhou, X. Y. Kong, G. Xie, P. Li, Z. Zhang, L. Wen and L. Jiang, *ACS Nano*, 2016, **10**, 9703-9709.

23. C. Ying, J. Houghtaling, O. M. Eggenberger, A. Guha, P. Nirmalraj, S. Awasthi, J. Tian and M. Mayer, *ACS Nano*, 2018, **12**, 11458-11470.

24. H. Kwok, K. Briggs and V. Tabard-Cossa, *PLoS One*, 2014, **9**, e92880.

25. E. Ferain and R. Legras, *Nucl. Instrum. Methods Phys. Res., B*, 2003, **208**, 115-122.

26. L. Piraux, V.-A. Antohe, E. Ferain and D. Lahem, *RSC Adv.*, 2016, **6**, 21808-21813.

27. E. Araujo, A. Encinas, Y. Velazquez-Galvan, J. M. Martinez-Huerta, G. Hamoir, E. Ferain and L. Piraux, *Nanoscale*, 2015, **7**, 1485-1490.

28. A. Vlad, V.-A. Antohe, J. M. Martinez-Huerta, E. Ferain, J.-F. Gohy and L. Piraux, *J. Mater. Chem. A*, 2016, **4**, 1603-1607.

29. L. Movsesyan, I. Schubert, L. Yeranyan, C. Trautmann and M. Eugenia Toimil-Molares, *Semicond. Sci. Technol.*, 2016, **31**, 014006.

30. D. Lefèvre, J. Louvegny, M. Naudin, E. Ferain, C. Dupont-Gillain and S. Demoustier-Champagne, *RSC Adv.*, 2018, **8**, 22932-22943.

31. D. Stein, M. Kruithof and C. Dekker, *Phys. Rev. Lett.*, 2004, **93**, 035901.

32. E. T. Acar, S. F. Buchsbaum, C. Combs, F. Fornasiero and Z. S. Siwy, *Sci. Adv.*, 2019, **5**, eaav2568.

33. G. Pérez-Mitta, C. Trautmann, E. Toimil-Molares and O. Azzaroni, in *Chemically Modified Nanopores and Nanochannels*, eds. M. Tagliazucchi and I. Szleifer, William Andrew, Oxford, United Kingdom, 2017, pp. 61-83.

34. H. Zhang, Y. Tian and L. Jiang, *Nano Today*, 2016, **11**, 61-81.

35. K. Xiao, L. Wen and L. Jiang, *Small*, 2016, **12**, 2810-2831.

36. P. Y. Apel, Y. E. Korchev, Z. Siwy, R. Spohr and M. Yoshida, *Nucl. Instrum. Meth. B*, 2001, **184**, 337-346.

37. P. Y. Apel, I. V. Blonskaya, A. Y. Didyk, S. N. Dmitriev, O. L. Orelovitch, D. Root, L. I. Samoilova and V. A. Vutsadakis, *Nucl. Instrum. Meth. B*, 2001, **179**, 55-62.

38. M. Ali, P. Ramirez, H. Q. Nguyen, S. Nasir, J. Cervera, S. Mafe and W. Ensinger, *ACS Nano*, 2012, **6**, 3631-3640.

39. D. Mo, J. D. Liu, J. L. Duan, H. J. Yao, H. Latif, D. L. Cao, Y. H. Chen, S. X. Zhang, P. F. Zhai and J. Liu, *Nucl. Instrum. Meth. B*, 2014, **333**, 58-63.

40. S. De, A. Patel and J. L. Lutkenhaus, *J. Mater. Res.*, 2020, **35**, 1163-1172.

41. S. R. Kwon, M. B. Elinski, J. D. Batteas and J. L. Lutkenhaus, *ACS Appl. Mater. Interfaces*, 2017, **9**, 17125-17135.

42. S. R. Kwon, J.-W. Jeon and J. L. Lutkenhaus, *RSC Adv.*, 2015, **5**, 14994-15001.

43. L. Shao, J.-W. Jeon and J. L. Lutkenhaus, *J. Mater. Chem. A*, 2013, **1**, 7648-7656.

44. S. Peralta, J. L. Habib-Jiwan and A. M. Jonas, *Chemphyschem*, 2009, **10**, 137-143.

45. E. Nicol, A. Moussa, J. L. Habib-Jiwan and A. M. Jonas, *J. Photochem. Photobiol.*, 2004, **167**, 31-35.

46. J. Yun, I. Echols, P. Flouda, S. Wang, A. Easley, X. Zhao, Z. Tan, E. Prehn, G. Zi, M. Radovic, M. J. Green and J. L. Lutkenhaus, *ACS Appl. Mater. Interfaces*, 2019, **11**, 47929-47938.

47. B. Katana, P. Rouster, G. Varga, S. Muráth, K. Glinel, A. M. Jonas and I. Szilagyi, *ACS Appl. Bio Mater.*, 2019, **3**, 522-530.

48. A. Vander Straeten, A. Bratek-Skicki, A. M. Jonas, C. A. Fustin and C. Dupont-Gillain, *ACS Nano*, 2018, **12**, 8372-8381.

49. D. G. Ramírez-Wong, C. Coelho-Diogo, C. Aimé, C. Bonhomme, A. M. Jonas and S. Demoustier-Champagne, *Appl. Surf. Sci.*, 2015, **338**, 154-162.

50. A. Vander Straeten, D. Lefevre, S. Demoustier-Champagne and C. Dupont-Gillain, *Adv. Colloid Interface Sci.*, 2020, **280**, 102161.

51. S. T. Dubas and J. B. Schlenoff, *Macromolecules*, 1999, **32**, 8153-8160.

52. K. Glinel, A. Moussa, A. M. Jonas and A. Laschewsky, *Langmuir*, 2002, **18**, 1408-1412.

53. M. H. Iqbal, A. Schroder, H. Kerdjoudj, C. Njel, B. Senger, V. Ball, F. Meyer and F. Boulmedais, *ACS Appl. Mater. Interfaces*, 2020, **12**, 22601-22612.

54. H. L. Tan, M. J. McMurdo, G. Pan and P. G. Van Patten, *Langmuir*, 2003, **19**, 9311-9314.

55. E. Poptoshev, B. Schoeler and F. Caruso, *Langmuir*, 2004, **20**, 829-834.

56. L. Zhang, H. Liu, E. Zhao, L. Qiu, J. Sun and J. Shen, *Langmuir*, 2012, **28**, 1816-1823.

57. J. Zhao, F. Pan, P. Li, C. Zhao, Z. Jiang, P. Zhang and X. Cao, *ACS Appl. Mater. Interfaces*, 2013, **5**, 13275-12383.

58. X. Wang, K. Naka, H. Itoh, T. Uemura and Y. Chujo, *Macromolecules*, 2003, **36**, 533-535.

59. G. V. Dubacheva, P. Dumy, R. Auzély, P. Schaaf, F. Boulmedais, L. Jierry, L. Coche-Guerente and P. Labbé, *Soft Matter*, 2010, **6**, 3747-3750.

60. Y. Tian, Q. He, C. Tao and J. Li, *Langmuir*, 2006, **22**, 360-362.

61. Y. W. Chu, B. Y. Wang, H. S. Lin, T. Y. Lin, Y. J. Hung, D. A. Engebretson, W. Lee and J. R. Carey, *Chem. Commun.*, 2013, **49**, 2397-2399.

62. O. Azzaroni, M. Álvarez, A. I. Abou-Kandil, B. Yameen and W. Knoll, *Adv. Funct. Mater.*, 2008, **18**, 3487-3496.

63. D. Pallarola, N. Queralto, W. Knoll, M. Ceolin, O. Azzaroni and F. Battaglini, *Langmuir*, 2010, **26**, 13684-13696.

64. D. Pallarola, N. Queralto, W. Knoll, O. Azzaroni and F. Battaglini, *Chem. Eur. J.*, 2010, **16**, 13970-13975.

65. D. Pallarola, N. Queralto, F. Battaglini and O. Azzaroni, *Phys. Chem. Chem. Phys.*, 2010, **12**, 8071-8083.

66. Y. Ko, H. Baek, Y. Kim, M. Yoon and J. Cho, *ACS Nano*, 2013, **7**, 143-153.

67. Y. Ko, M. Kwon, W. K. Bae, B. Lee, S. W. Lee and J. Cho, *Nat. Commun.*, 2017, **8**, 536.

68. F. Zhang and M. P. Srinivasan, *Langmuir*, 2007, **23**, 10102-10108.

69. Y. Ko, C. H. Kwon, S. W. Lee and J. Cho, *Adv. Mater.*, 2020, **32**, e2001924.

70. M. Tagliazucchi, O. Azzaroni and I. Szleifer, *J. Am. Chem. Soc.*, 2010, **132**, 12404-12411.

71. S. Cuenot, S. Radji, H. Alem, S. Demoustier-Champagne and A. M. Jonas, *Small*, 2012, **8**, 2978-2985.

72. S. Radji, H. Alem, S. Demoustier-Champagne, A. M. Jonas and S. Cuenot, *Macromol. Chem. Phys.*, 2012, **213**, 580-586.

73. Y. Wu, Q. Gu, G. Ding, F. Tong, Z. Hu and A. M. Jonas, *ACS Macro Lett.*, 2013, **2**, 535-538.

74. T. D. Lazzara, K. H. Lau, A. I. Abou-Kandil, A. M. Caminade, J. P. Majoral and W. Knoll, *ACS Nano*, 2010, **4**, 3909-3920.

75. A. Pallandre, A. Moussa, B. Nysten and A. M. Jonas, *Adv. Mater.*, 2006, **18**, 481-486.

76. Y. Cho, C. Lee and J. Hong, *Colloids Surf. A Physicochem. Eng. Asp.*, 2014, **443**, 195-200.

77. Y. Cho, J. Lim and K. Char, *Soft Matter*, 2012, **8**, 10271-10278.

78. Y. Cho, W. Lee, Y. K. Jhon, J. Genzer and K. Char, *Small*, 2010, **6**, 2683-2689.

79. J. P. DeRocher, P. Mao, J. Han, M. F. Rubner and R. E. Cohen, *Macromolecules*, 2010, **43**, 2430-2437.

80. D. Lee, A. J. Nolte, A. L. Kunz, M. F. Rubner and R. E. Cohen, *J. Am. Chem. Soc.*, 2006, **128**, 8521-8529.

81. S. Ai, G. Lu, Q. He and J. Li, *J. Am. Chem. Soc.*, 2003, **125**, 11140-11141.

82. H. Alem, F. Blondeau, K. Glinel, S. Demoustier-Champagne and A. M. Jonas, *Macromolecules*, 2007, **40**, 3366-3372.

83. D. Lee, R. E. Cohen and M. F. Rubner, *Langmuir*, 2007, **23**, 123-129.

84. S. Ai, Q. He, C. Tao, S. Zheng and J. Li, *Macromol. Rapid Commun.*, 2005, **26**, 1965-1969.

85. S. Zhang, S. Demoustier-Champagne and A. M. Jonas, *Biomacromolecules*, 2015, **16**, 2382-2393.

86. M. V. Kiryukhin, S. M. Man, A. V. Sadovoy, H. Y. Low and G. B. Sukhorukov, *Langmuir*, 2011, **27**, 8430-8436.

87. P. J. Yoo, K. T. Nam, A. M. Belcher and P. T. Hammond, *Nano Lett.*, 2008, **8**, 1081-1089.

88. C. Gao, B. Wang, J. Feng and J. Shen, *Macromolecules*, 2004, **37**, 8836-8839.

89. X. Chen, J. Sun and J. Shen, *Langmuir*, 2009, **25**, 3316-3320.

90. L. Asor, S. Nir, M. Oded, M. Reches and R. Shenhar, *Polymer*, 2017, **126**, 56-64.

91. J. C. Roy, C. C. Buron, S. Demoustier-Champagne and M. A. Jonas, in *Multilayer Thin Films: Sequential Assembly of Nanocomposite Materials*, eds. G. Decher and B. J. Schlenoff, Wiley-VCH Verlag & Co. KGaA, Weinheim, Germany, 2nd edn., 2012, pp. 613-634.

92. M. Y. Shen, S. Yuran, Y. Aviv, H. Ayalew, C. H. Luo, Y. H. Tsai, M. Reches, H. H. Yu and R. Shenhar, *ACS Appl. Mater. Interfaces*, 2019, **11**, 1201-1208.

93. M. Oded, A. H. Muller and R. Shenhar, *Soft Matter*, 2016, **12**, 8098-8103.

94. M. Oded, S. T. Kelly, M. K. Gilles, A. H. E. Müller and R. Shenhar, *Polymer*, 2016, **107**, 406-414.

95. M. Oded, S. T. Kelly, M. K. Gilles, A. H. Muller and R. Shenhar, *Soft Matter*, 2016, **12**, 4595-4602.

96. A. Pallandre, K. Glinel, A. M. Jonas and B. Nysten, *Nano Lett.*, 2004, **4**, 365-371.

97. J. B. Gilbert, J. S. O'Brien, H. S. Suresh, R. E. Cohen and M. F. Rubner, *Adv. Mater.*, 2013, **25**, 5948-5952.

98. S. Saghazadeh, S. Zhang, D. Lefevre, A. Le Beulze, A. M. Jonas and S. Demoustier-Champagne, *Langmuir*, 2015, **31**, 7264-7273.

99. S. Zhang, C. Vlemincq, D. Ramirez Wong, D. Magnin, K. Glinel, S. Demoustier-Champagne and A. M. Jonas, *J. Mater. Chem. B*, 2016, **4**, 7651-7661.

100. D. M. Kalaskar, C. Poleunis, C. Dupont-Gillain and S. Demoustier-Champagne, *Biomacromolecules*, 2011, **12**, 4104-4111.

101. W. Xu, E. Ferain, S. Demoustier-Champagne, K. Glinel and A. M. Jonas, *ACS Appl. Polym. Mater.*, 2019, **1**, 2407-2416.

102. X. Qu and T. Komatsu, *ACS Nano*, 2010, **4**, 563-573.

103. K. Glinel, A. Behrens, R. S. Langer, A. Jaklenec and A. M. Jonas, *Biomacromolecules*, 2019, **20**, 102-108.

104. S. Hou, J. Wang and C. R. Martin, *Nano Lett.*, 2005, **5**, 231-234.

105. R. Adachi, M. Akiyama, Y. Morita and T. Komatsu, *Chem. Asian J.*, 2018, **13**, 2796-2799.

106. T. Komatsu, T. Sato and C. Boettcher, *Chem. Asian J.*, 2012, **7**, 201-206.

107. S. Goto, Y. Amano, M. Akiyama, C. Bottcher and T. Komatsu, *Langmuir*, 2013, **29**, 14293-14300.

108. E. Colaco, D. Lefevre, E. Maisonhaute, D. Brouri, C. Guibert, C. Dupont-Gillain, K. El Kirat, S. Demoustier-Champagne and J. Landoulsi, *Nanoscale*, 2020, **12**, 10051-10064.

109. B. Chen, Y. Jia, J. Zhao, H. Li, W. Dong and J. Li, *J. Phys. Chem. C*, 2013, **117**, 19751-19758.

110. Q. He, H. Mohwald and J. Li, *Macromol. Rapid. Commun.*, 2009, **30**, 1538-1542.

111. Y. Amano and T. Komatsu, *Chem. Lett.*, 2015, **44**, 1646-1648.

112. T. Komatsu, H. Terada and N. Kobayashi, *Chem. Eur. J.*, 2011, **17**, 1849-1854.

113. N. Sugai, Y. Nakai, Y. Morita and T. Komatsu, *ACS Appl. Nano Mater.*, 2018, **1**, 3080-3085.

114. N. Sugai, Y. Morita and T. Komatsu, *Chem. Asian J.*, 2019, **14**, 2953-2957.

115. Y. Nakai, N. Sugai, H. Kusano, Y. Morita and T. Komatsu, *ACS Appl. Nano Mater.*, 2019, **2**, 4891-4899.

116. R. Kato and T. Komatsu, *J. Inorg. Organomet. Polym. Mater.*, 2012, **23**, 167-171.

117. X. Qu, N. Kobayashi and T. Komatsu, *ACS Nano*, 2010, **4**, 1732-1738.

118. T. Komatsu and N. Kobayashi, *Polym. Adv. Technol.*, 2011, **22**, 1315-1318.

119. S. Yuge, M. Akiyama and T. Komatsu, *Chem. Commun.*, 2014, **50**, 9640-9643.

120. S. Yuge, M. Akiyama, M. Ishii, H. Namkoong, K. Yagi, Y. Nakai, R. Adachi and T. Komatsu, *Chem. Lett.*, 2017, **46**, 95-97.

121. T. Komatsu, X. Qu, H. Ihara, M. Fujihara, H. Azuma and H. Ikeda, *J. Am. Chem. Soc.*, 2011, **133**, 3246-3248.

122. S. Kobayakawa, Y. Nakai, M. Akiyama and T. Komatsu, *Chem. Eur. J.*, 2017, **23**, 5044-5050.

123. B. G. Nair, Y. Nakano, Y. Ito and H. Abe, *Chem. Commun.*, 2014, **50**, 602-604.

124. W. Wang, Z. Wu, X. Lin, T. Si and Q. He, *J. Am. Chem. Soc.*, 2019, **141**, 6601-6608.

125. J. Li, Y. Jia, W. Dong, X. Feng, J. Fei and J. Li, *Nano Lett.*, 2014, **14**, 6160-6164.

126. D. G. Ramirez-Wong, S. Saghazadeh, S. Van Herck, B. G. De Geest, A. M. Jonas and S. Demoustier-Champagne, *Biomacromolecules*, 2017, **18**, 4299-4306.

127. Z. Wu, Y. Wu, W. He, X. Lin, J. Sun and Q. He, *Angew. Chem. Int. Ed.*, 2013, **52**, 7000-7003.

128. C. J. Roy, N. Chorine, B. G. De Geest, S. De Smedt, A. M. Jonas and S. Demoustier-Champagne, *Chem. Mater.*, 2012, **24**, 1562-1567.

129. B. G. De Geest, C. Dejugnat, E. Verhoeven, G. B. Sukhorukov, A. M. Jonas, J. Plain, J. Demeester and S. C. De Smedt, *J. Control Release*, 2006, **116**, 159-169.

130. B. G. De Geest, A. M. Jonas, J. Demeester and S. C. De Smedt, *Langmuir*, 2006, **22**, 5070-5074.

131. J. Zhou, M. V. Pishko and J. L. Lutkenhaus, *Langmuir*, 2014, **30**, 5903-5910.

132. Z. Wu, C. Gao, J. Frueh, J. Sun and Q. He, *Macromol. Rapid Commun.*, 2015, **36**, 1444-1449.

133. K. K. Chia, M. F. Rubner and R. E. Cohen, *Langmuir*, 2009, **25**, 14044-14052.

134. R. Kato and T. Komatsu, *Chem. Lett.*, 2011, **40**, 1338-1339.

135. S. Rajesh, Y. Yan, H. C. Chang, H. Gao and W. A. Phillip, *ACS Nano*, 2014, **8**, 12338-12345.

136. G. Li, J. Fei, Y. Xu, Y. Li and J. Li, *Adv. Funct. Mater.*, 2018, **28**, 1706557.

137. O. Azzaroni and K. H. Lau, *Soft Matter*, 2011, **7**, 8709-8724.

138. C. A. Ghiorghita and M. Mihai, *Chemosphere*, 2020, **270**, 129477.

139. M. A. Mokhter, S. Lakard, C. Magnenet, M. Euvrard and B. Lakard, *Environ. Technol.*, 2017, **38**, 2476-2485.

140. N. Joseph, P. Ahmadiannamini, R. Hoogenboom and I. F. J. Vankelecom, *Polym. Chem.*, 2014, **5**, 1817-1831.

141. S. K. Kumar and J. D. Hong, *Langmuir*, 2008, **24**, 4190-4193.

142. M. Ali, B. Yameen, J. Cervera, P. Ramirez, R. Neumann, W. Ensinger, W. Knoll and O. Azzaroni, *J. Am. Chem. Soc*, 2010, **132**, 8338-8348.

143. G. Pérez-Mitta, A. Albesa, F. M. Gilles, M. E. Toimil-Molares, C. Trautmann and O. Azzaroni, *J. Phys. Chem. C*, 2017, **121**, 9070-9076.

144. J. Li, P. An, C. Qin, C. L. Sun, M. Sun, Z. Ji, C. Wang, G. Du, J. Liu and Y. Xie, *ACS Omega*, 2020, **5**, 4501-4506.

145. S. Zhang, L. Yang, D. Ding, P. Gao, F. Xia and M. L. Bruening, *Anal. Chem.*, 2021, **93**, 4291-4298.

146. A. Santos, T. Kumeria and D. Losic, *TrAC Trends Anal. Chem.*, 2013, **44**, 25-38.

147. M. Ali, B. Yameen, R. Neumann, W. Ensinger, W. Knoll and O. Azzaroni, *J. Am. Chem. Soc.*, 2008, **130**, 16351-16357.

148. G. Perez-Mitta, A. S. Peinetti, M. L. Cortez, M. E. Toimil-Molares, C. Trautmann and O. Azzaroni, *Nano Lett.*, 2018, **18**, 3303-3310.

149. C. Y. Lin, C. Combs, Y. S. Su, L. H. Yeh and Z. S. Siwy, *J .Am. Chem. Soc.*, 2019, **141**, 3691-3698.

150. L. Ouyang, R. Malaisamy and M. L. Bruening, *J. Membr. Sci.*, 2008, **310**, 76-84.

151. B. P. Tripathi, N. C. Dubey and M. Stamm, *J. Hazard Mater.*, 2013, **252-253**, 401-412.

152. R. Malaisamy and M. L. Bruening, *Langmuir*, 2005, **21**, 10587-12592.

153. C. Magnenet, S. Lakard, C. C. Buron and B. Lakard, *J. Colloid Interface Sci.*, 2012, **376**, 202-208.

154. E. Halakoo and X. Feng, *Sep. Purif. Technol.*, 2020, **234**, 116077.

155. A. Toutianoush, W. Jin, H. Deligöz and B. Tieke, *Appl. Surf. Sci.*, 2005, **246**, 437-443.

156. Q. Nan, P. Li and B. Cao, *Appl. Surf. Sci.*, 2016, **387**, 521-528.

157. M. G. Bisheh, M. Ghorbani, M. Peyravi and M. Jahanshahi, *Chem. Eng. Res. Des.*, 2020, **153**, 829-838.

158. A. El-Hashani, A. Toutianoush and B. Tieke, *J. Membr. Sci.*, 2008, **318**, 65-70.

159. A. Prasannan, J. Udomsin, H.-C. Tsai, C.-F. Wang and J.-Y. Lai, *Chem. Eng. J.*, 2020, **391**, 123585.

160. K. L. Cho, H. Lomas, A. J. Hill, F. Caruso and S. E. Kentish, *Langmuir*, 2014, **30**, 8784-8790.

161. M. Arslan, G. Dönmez, A. Ergün, M. Okutan, G. Albayrak Arı and H. Deligöz, *Polym. Eng. Sci.*, 2019, **60**, 341-351.

162. M.-Y. Xie, J. Wang and Q.-Y. Wu, *Chinese J. Polym. Sci.*, 2020, **38**, 965-972.

163. X. Li, Y. Xu, K. Goh, T. H. Chong and R. Wang, *J. Membr. Sci.*, 2020, **615**, 118514.

164. Y. Liu, S. Zheng, P. Gu, A. J. Ng, M. Wang, Y. Wei, J. J. Urban and B. Mi, *Carbon*, 2020, **160**, 219-227.

165. C. Cheng, N. White, H. Shi, M. Robson and M. L. Bruening, *Polymer*, 2014, **55**, 1397-1403.

166. N. White, M. Misovich, E. Alemayehu, A. Yaroshchuk and M. L. Bruening, *Polymer*, 2016, **103**, 478-485.

167. S. U. Hong, R. Malaisamy and M. L. Bruening, *J. Membr. Sci.*, 2006, **283**, 366-372.

168. Y. Zhao, K. Tang, H. Liu, B. Van der Bruggen, A. Sotto Díaz, J. Shen and C. Gao, *J. Membr. Sci.*, 2016, **520**, 262-271.

169. L. Yang, C. Tang, M. Ahmad, A. Yaroshchuk and M. L. Bruening, *ACS Appl. Mater. Interfaces*, 2018, **10**, 44134-44143.

170. K. L. Cho, A. J. Hill, F. Caruso and S. E. Kentish, *Adv. Mater.*, 2015, **27**, 2791-2796.

171. S. Abdu, M. C. Marti-Calatayud, J. E. Wong, M. Garcia-Gabaldon and M. Wessling, *ACS Appl. Mater. Interfaces*, 2014, **6**, 1843-1854.

172. S. U. Hong, R. Malaisamy and M. L. Bruening, *Langmuir*, 2007, **23**, 1716-1722.

173. A. M. Balachandra, J. Dai and M. L. Bruening, *Macromolecules*, 2002, **35**, 3171-3178.

174. S. U. Hong and M. L. Bruening, *J. Membr. Sci.*, 2006, **280**, 1-5.

175. X. Y. Liu and M. L. Bruening, *Chem. Mater.*, 2004, **16**, 351-357.

176. D. Kim, P. Tzeng, K. J. Barnett, Y. H. Yang, B. A. Wilhite and J. C. Grunlan, *Adv. Mater.*, 2014, **26**, 746-751.

177. F. Xiang, A. M. Marti and D. P. Hopkinson, *J. Membr. Sci.*, 2018, **556**, 146-153.

178. N. B. Pramanik and S. L. Regen, *Chem. Commun.*, 2019, **55**, 4347-4350.

179. D. M. Sullivan and M. L. Bruening, *Chem. Mater.*, 2003, **15**, 281-287.

180. K. Remmen, R. Schäfer, S. Hedwig, T. Wintgens, M. Wessling and M. Lenz, *Environ. Sci. Water Res. Technol.*, 2019, **5**, 1683-1688.

181. L. Paltrinieri, K. Remmen, B. Müller, L. Chu, J. Köser, T. Wintgens, M. Wessling, L. C. P. M. de Smet and E. J. R. Sudhölter, *J. Membr. Sci.*, 2019, **587**, 117162.

182. S. Ilyas, J. de Grooth, K. Nijmeijer and W. M. de Vos, *J. Colloid Interface Sci.*, 2015, **446**, 386-393.

183. N. Dizge, R. Epsztein, W. Cheng, C. J. Porter and M. Elimelech, *J. Membr. Sci.*, 2018, **549**, 357-365.

184. L. Shen, X. Cui, G. Yu, F. Li, L. Li, S. Feng, H. Lin and J. Chen, *J. Colloid Interface Sci.*, 2017, **494**, 194-203.

185. M. Son, W. Yang, S. S. Bucs, M. F. Nava-Ocampo, J. S. Vrouwenvelder and B. E. Logan, *Environ. Sci. Technol. Lett.*, 2018, **5**, 584-590.

186. L. Shan, H. Guo, Z. Qin, N. Wang, S. Ji, G. Zhang and Z. Zhang, *RSC Adv.*, 2015, **5**, 11515-11523.

187. X. Zhao, A. Qin, D. Liu and C. He, *RSC Adv.*, 2015, **5**, 63580-63587.

188. E. V. Pasco, H. Shi, I. Xagoraraki, S. A. Hashsham, K. N. Parent, M. L. Bruening and V. V. Tarabara, *J. Membr. Sci.*, 2014, **469**, 140-150.

189. M. Ji, X. Li, M. Omidvarkordshouli, S. B. Sigurdardóttir, J. M. Woodley, A. E. Daugaard, J. Luo and M. Pinelo, *Sep. Purif. Technol.*, 2020, **247**, 116936.

190. J. A. Armstrong, E. E. Bernal, A. Yaroshchuk and M. L. Bruening, *Langmuir*, 2013, **29**, 10287-10296.

191. D. Constantin and Z. S. Siwy, *Phys. Rev. E*, 2007, **76**, 041202.

192. R. Sarma, M. S. Islam, A. F. Miller and D. Bhattacharyya, *ACS Appl. Mater. Interfaces*, 2017, **9**, 14858-14867.

193. L. Yang, L. Bui, D. Hanjaya-Putra and M. L. Bruening, *Anal. Chem.*, 2020, **92**, 11912-11920.

194. S. Datta, C. Cecil and D. Bhattacharyya, *Ind. Eng. Chem. Res.*, 2008, **47**, 4586-4597.

195. D. M. Dotzauer, S. Bhattacharjee, Y. Wen and M. L. Bruening, *Langmuir*, 2009, **25**, 1865-1871.

196. D. M. Dotzauer, J. Dai, L. Sun and M. L. Bruening, *Nano Lett.*, 2006, **6**, 2268-2272.

197. H. Shen, J. Watanabe and M. Akashi, *Polym. J.*, 2010, **43**, 35-40.

198. W. Knoll, O. Azzaroni, H. Duran, J. Kunze-Liebhauser, K. H. A. Lau, E. Reimhult and B. Yameen, *Anal. Bioanal. Chem.*, 2020, **412**, 3299-3315.

199. J. Dai, G. L. Baker and M. L. Bruening, *Anal. Chem.*, 2006, **78**, 135-140.

200. K. Hotta, A. Yamaguchi and N. Teramae, *J. Phys. Chem. C*, 2012, **116**, 23533-23539.

201. Z. Siwy, E. Heins, C. C. Harrell, P. Kohli and C. R. Martin, *J. Am. Chem. Soc.*, 2004, **126**, 10850-10851.

202. M. Gao, P. C. Tsai, Y. S. Su, P. H. Peng and L. H. Yeh, *Small*, 2020, **16**, e2006013.

203. D. C. Zheng and L. H. Yeh, *Micromachines*, 2020, **11**, 949.

204. Y. Ai, M. Zhang, S. W. Joo, M. A. Cheney and S. Qian, *J. Phys. Chem. C*, 2010, **114**, 3883-3890.

205. X. Zhu, J. Hao, B. Bao, Y. Zhou, H. Zhang, J. Pang, Z. Jiang and L. Jiang, *Sci. Adv.*, 2018, **4**, eaau1665.

206. S. Lee, B. Lee, B. J. Kim, J. Park, M. Yoo, W. K. Bae, K. Char, C. J. Hawker, J. Bang and J. Cho, *J. Am. Chem. Soc.*, 2009, **131**, 2579-2587.